



## Role of electronic energy loss on defect production and interface stability: Comparison between ceramic materials and high-entropy alloys<sup>☆</sup>

Yanwen Zhang <sup>a,b,\*</sup>, Chinthaka Silva <sup>a,c</sup>, Timothy G. Lach <sup>a</sup>, Matheus A. Tunes <sup>d,e</sup>, Yufan Zhou <sup>a</sup>, Lauren Nuckols <sup>b</sup>, Walker L. Boldman <sup>b</sup>, Philip D. Rack <sup>b,f</sup>, Stephen E. Donnelly <sup>d</sup>, Li Jiang <sup>g</sup>, Lumin Wang <sup>g</sup>, William J. Weber <sup>b</sup>

<sup>a</sup> Materials Science and Technology Division, Oak Ridge National Laboratory, Oak Ridge, TN 37831, USA

<sup>b</sup> Department of Materials Science & Engineering, University of Tennessee, Knoxville, TN 37996, USA

<sup>c</sup> Chemistry of Nuclear Materials, Lawrence Livermore National Laboratory, 7000 East Avenue, Livermore, CA 94550, USA

<sup>d</sup> School of Computing and Engineering, University of Huddersfield, Huddersfield HD1 3DH, UK

<sup>e</sup> Materials Science and Technology Division, Los Alamos National Laboratory, Los Alamos, NM 87545, USA

<sup>f</sup> Center for Nanophase Materials Sciences, Oak Ridge National Laboratory, Oak Ridge, TN 37831, USA

<sup>g</sup> Department of Nuclear Engineering and Radiological Sciences, University of Michigan, Ann Arbor, MI 48109, USA



### ARTICLE INFO

#### Keywords:

Radiation damage  
High-entropy alloys  
Chemically complex alloys, nanocrystalline alloys  
Crystallites  
Electronic energy loss  
Displacement damage, grain growth

### ABSTRACT

High-entropy alloys (HEAs) and some complex alloys exhibit desirable properties and significant structural stability in harsh environments, including possible applications in advanced reactors. Energetic ion irradiation is often used as a surrogate for neutron irradiation; however, the impact of ion electronic energy deposition and dissipation is often neglected. Moreover, differences in recoil energy spectrum and density of cascade events on damage evolution must also be considered. In many chemically complex alloys, the mean free path of electrons is reduced significantly, thus their decreased thermal conductivity and slow dissipation of localized radiation energy can have noticeable effects on displacement cascade evolution that is greatly different from metals with high thermal conductivity. In this work, nanocrystalline HEAs of Ni<sub>20</sub>Fe<sub>20</sub>Co<sub>20</sub>Cr<sub>20</sub>Cu<sub>20</sub> and nonequimolar (NiFe-CoCr)<sub>97</sub>Cu<sub>3</sub>, both having much lower room-temperature thermal conductivity than pure Ni or Fe, are chosen as model HEAs to reveal the role that electronic energy loss during ion irradiation has in complex alloys. The response of nanocrystalline HEAs is investigated under irradiation at room temperature using MeV Ni and Au ions that have different ratios of electronic energy to damage energy, which is the energy dissipated in displacing atoms. Different from previously reported amorphization of nanocrystalline SiC, experimental results on these HEAs show that, similar to the process in nanocrystalline oxide materials, both inelastic thermal spikes via electron-phonon coupling and elastic thermal spikes via collisions among atomic nuclei contribute to the overall grain growth. The growth follows a power law dependence with the total deposited ion energy, and the derived value of the power-exponent suggests that the irradiation-induced instability at and near grain boundaries leads to local rapid atomic rearrangements and consequently grain growth. The high power-exponent value can be attributed to the sluggish diffusion and delayed defect evolution arising from the chemical complexity intrinsic to HEAs. This work calls attention to quantified fundamental understanding of radiation damage processes beyond that of simplified displacement events, especially in simulating neutron environments.

<sup>☆</sup> Notice: This manuscript has been authored by UT-Battelle, LLC, under contract DE-AC05-00OR22725 with the US Department of Energy (DOE). The US government retains and the publisher, by accepting the article for publication, acknowledges that the US government retains a nonexclusive, paid-up, irrevocable, worldwide license to publish or reproduce the published form of this manuscript, or allow others to do so, for US government purposes. DOE will provide public access to these results of federally sponsored research in accordance with the DOE Public Access Plan (<https://energy.gov/downloads/doe-public-access-plan>).

\* Corresponding author.

E-mail address: [Zhangy1@ornl.gov](mailto:Zhangy1@ornl.gov) (Y. Zhang).

## 1. Introduction

To address the abundant challenges in developing structural alloys for next-generation nuclear power systems, the promising properties resulting from the tunable chemical complexity in concentrated solid-solution alloys (CSAs) and high-entropy alloys (HEAs) have recently attracted increasing attention [1,2]. While neutron exposure is a critical test for any structural alloys to be considered viable for reactor applications, limitation in achievable high damage levels to evaluate the performance of candidate alloys is a bottleneck. Ion irradiation is the most amenable method to reach high doses in a reasonable time, for example producing tens to hundreds of displacements per atom (dpa) in a few hours; thus, energetic ions are often used as a surrogate for neutrons that has greatly accelerated the research and development (R&D) processes for investigating radiation effects in materials [3–5].

Alloys in radiation environments undergo structural damage and property degradation [6]. Radiation damage in dilute alloys has been investigated intensively for over 70 years. In dilute alloys, solute elements are expected to effectively trap irradiation-induced defects and pin dislocations and impede their movement [6–11]. At elevated temperatures, because of preferential and directional diffusion biases, different elemental species (i.e., solute and solvent atoms, as well as point defects and defect clusters) migrate at different rates under ion irradiation, resulting in radiation-induced segregation, precipitation, creep, embrittlement, and void swelling [11–14]. To further improve alloy performance in radiation environments, more recent research focuses on microstructural inhomogeneities, including embedded nanoclusters, secondary phases, grain boundaries (GBs), and interfaces. These inhomogeneities are introduced in dilute alloys to mitigate radiation-induced damage by providing a large number of defect sinks [14–19].

Conceptually different from dilute alloys, in which solute elements have few interactions among themselves, CSAs are composed of two or more principal elements at or close to equiatomic concentrations. In CSAs, long-range order (i.e., elemental sublattices) does not exist: all elements randomly distribute on lattice sites and each atom can have different neighbor configurations. Moreover, the same element likely exists at one or more nearest-neighbor positions, and the concept of solute–solvent interactions does not apply. HEAs, which can be considered as a subset of CSAs, commonly contain five or more elemental species [20–23]. In HEAs, the random arrangement of multiple elemental species creates solid-solution heterogeneities (i.e., chemical complexity) that lead to unique nonperiodic electronic structure and energy landscapes [1,24–26]. Results show that increases in chemical complexity can lead to notable reduction in mean free paths of electrons, phonons and magnons [25–27], as well as sluggish diffusion [28,29] and mass transport [26,29]. Such modifications at the level of electrons and atoms effectively impact both defect production and survival during energy dissipation on a femtosecond (fs) to picosecond (ps) time frame, and damage evolution over much longer time scales. Improved radiation performance in complex CSAs is attributed to locally slow heat dissipation, improved defect annealing and suppressed formation of extended defects at the early stages of radiation events, which consequentially reduce the number of surviving defects and slow down damage accumulation [1,26,51]. Tuning the chemical complexity resulting from the elemental heterogeneities allows tailoring of defect production and evolution in high-radiation environments [1,26,30–33], and represents a unique opportunity for structural alloys by design for nuclear applications [2].

Recent research looks beyond properties that are intrinsic to HEAs to include structural complexity (e.g., nanoscale features) for further property enhancement [34–40], similar to that done in dilute alloys to include nanoscale inhomogeneities [14–16]. These research efforts include alloying low concentrations of pinning sites in CSAs [41,42], high-density GBs and interfaces in the nanocrystalline form [43–47], and oxide-dispersion-strengthened HEAs [48,49]. Compared with

nanocrystalline dilute alloys, nanostructured HEAs are expected to be more stable under ion irradiation because of their combination of high-density interfaces and GBs and intrinsic properties such as slow heat dissipation [1,26,30], sluggish diffusion [28,29], and chemically biased mass transport [27], as well as suppressed damage accumulation [1].

Unlike neutron irradiation, ion irradiation has the advantages of well-controlled irradiation conditions (e.g., damage profiles, dose, dose rate, temperature) and easy sample handling (nonradioactive). Energetic ion beams are also an effective way to tailor size-dependent material properties [47,50,51] and to induce phase transformations via nonequilibrium processes [47,51]. While there are abundant ion irradiation effect studies in dilute alloys in the past over 70 year and several studies on ion irradiation induced grain growth in nanocrystalline dilute alloys or metals [52–54] and oxides [55–59], the efforts have been generally focused only on the effects of displacement damage [52–54]; whereas electronic effects [59,60], especially in metals and alloys, are largely overlooked [51]. An energetic ion inherently induces a simultaneous disturbance of the electronic and atomic subsystems. While energy deposited into the atomic subsystem is dissipated through elastic atomic collisions and phonons resulting in displaced atoms and local heating (i.e., elastic thermal spikes), the energy deposited into the electronic subsystem causes extreme ionization that is dissipated to the atomic subsystem via electron–phonon coupling (i.e., inelastic thermal spike along the ion path), leading to enhanced defect and atomic diffusion that affects atomic processes and microstructural evolutions. It is commonly accepted that electrons in metal and alloys are delocalized, and heat is mainly conducted via free electrons. However, electrons in CSAs with high chemical complexity may be localized [1,26], which leads to significant reduction of the mean free path of electrons [1,26,30,61]. Research has shown that the mean free path in different Ni-based CSAs is much shorter than that in pure Ni metal with free electrons [1], and alloying with Cr significantly lowers the thermal conductivity, which is attributed to electronic deformation [26,61]. Electronic energy deposition and dissipation have recently shown to lead to defect relaxation in NiFe and NiFeCoCr CSAs, determined from x-ray diffraction (XRD) measurements [32], transmission electron microscopy (TEM) characterization [62], and molecular dynamic simulations [63]. Compared with nanocrystalline dilute alloys or bulk CSAs, nanostructured HEAs are expected to be more stable under ion irradiation because of their combination of a high density of microstructural inhomogeneities (e.g., interfaces and grain boundaries) and intrinsic properties (e.g., slow heat dissipation, sluggish diffusion, and chemically biased mass transport, as well as suppressed damage accumulation). It is worth noting that reduction in thermal conductivity is evident in many complex alloys, and even in some conventional alloys. As pointed out in previous work [30], solid solution disorder can effectively modify electronic and atomic properties, which affect energy transport under irradiation, either directly via decreases in electron mean free path or indirectly via changes in energy flow from electronic to atomic subsystem through electron–phonon coupling. Such modifications can have noticeable effects on displacement cascade evolution that is greatly different from metals with good thermal conductivity. As ion irradiation will continue to be a critical tool to evaluate performance of structural alloys in future reactor environments, the impact of electronic energy deposition and dissipation should be carefully considered.

Ion irradiation is a highly accelerated approach, and its relevance to fission and fusion neutron irradiations needs to be addressed. Furthermore, the large differences in temporal and spatial scales of ion and fission/fusion neutron irradiations are unique challenges. Well-controlled ion irradiation studies allow separate effects to be studied to delineate various contributions to material degradation. Using different ion masses, energies and fluxes, ion irradiation can cover a broad range of neutron recoil spectra and allow dose-rate studies, thus providing a path forward to emulate fission and fusion neutron regimes with confidence in order to develop strategies to enhance radiation tolerance (i.e., resist to degradation) and to predict material

performance. Keeping in mind that primary knock-on atoms (PKAs) from fusion neutrons (or spallation neutrons used to simulate fusion neutrons) can be several MeV, thus similar to ion irradiation. Nevertheless, new scientific perspectives of exploiting ions to accelerate the damage evolution in a neutron-relevant manner requires understanding and quantifying differences arising from the athermal effects [51] from hot electrons created along the trajectory of ions versus neutron generated PKAs, as well as from differences in recoil spectra and cascade density on damage evolution.

In this work, Ni self-ions and heavier Au ions, with energies of up to 23 MeV, were chosen to deposit electronic (ionizing) and damage energy into nanocrystalline HEAs—equiatomic  $\text{Ni}_{20}\text{Fe}_{20}\text{Co}_{20}\text{Cr}_{20}\text{Cu}_{20}$  (HEA-20Cu) and non-equiautomic ( $\text{NiFeCoCr})_{97}\text{Cu}_3$  (HEA-3Cu) films. The aim of using different ion masses and energies was to deposit ionizing energy and ballistic energy at different rates and ratios to both target electrons and nuclei, respectively. It is known that  $\text{Ni}_{25}\text{Fe}_{25}\text{Co}_{25}\text{Cr}_{25}$  (NiFeCoCr) is a single-phase face-centered cubic (fcc) solid solution with a much-reduced thermal conductivity than pure Ni or Fe resulting from alloying element Cr [61]. Furthermore, alloying with Cu stabilizes the crystalline structure to form fcc HEA-3Cu and HEA-20Cu. Nevertheless, due to its positive enthalpy of mixing with other alloying constituents and the tendency of phase separation, an additional fcc phase with local concentration variation may form [64,65], especially during thermal treatment or under irradiation. These intrinsic properties together with dense interfaces and GBs in their nanocrystalline form, make the alloys a good model system to demonstrate the non-negligible effects of ionization. Here the nanocrystalline HEA-3Cu and HEA-20Cu films are chosen to reveal ionization effects. Study of their irradiation performance and mechanism interpretation on GB stability, radiation-induced segregation, and precipitation will be the subject of future studies. The response of these model HEAs under ion beams was evaluated with a complementary set of experimental techniques and numerical analyses to understand the effects of ionizing inelastic thermal spikes and displacive elastic thermal spikes on the stability of nanostructured HEAs. In addition, grain growth of nanocrystalline ceramics and alloys, via thermal annealing or athermal processes under ion radiation, is briefly reviewed to provide an assessment of the electronic effects in comparison with the HEAs herein investigated. It is acknowledged that athermal processes often have little or weak dependence on temperature [51]. Knowledge of the stability of nanostructured HEAs to irradiation is essential to successful utilization of these materials in high-radiation environments and for a wide variety of applications. Understanding the critical roles that elemental and microstructural heterogeneities in HEAs play in responding to ionizing and displacing radiation may lead to transformative opportunities in materials research.

## 2. Experimental conditions, energy deposition, and characterization techniques

### 2.1. Film deposition

Nanocrystalline HEA-3Cu and HEA-20Cu films with thicknesses of about 1000 nm were sputter-deposited on  $\text{Si}(100)$  and  $\text{SiO}_2/\text{Si}(100)$  wafers, respectively [66,67]. The thin  $\text{SiO}_2$  layer was grown via thermal oxidation before the deposition of the HEA-20Cu films to minimize the influence of the substrate. While chemical complexity does not monotonically increase with the number of alloying elements, it does depend on the coupling strengths of constituents (i.e., electron, magnetic, and phonon interactions) [1]. Thus, the maximum chemical complexity may not occur at the maximum compositional disorder, which is the equiatomic composition. In equiatomic HEA-20Cu, there are 40% of Cr + Fe and 60% of Co + Ni + Cu, while in nonequiautomic HEA-3Cu, the corresponding percentages are 48.5% and 51.5%, respectively. Due to relatively lower Cr and Fe concentrations, 20% each, in HEA-20Cu, slightly reduced differences exist between the partially-filled and fully-filled  $d$  orbitals. In HEA-3Cu, the difference is larger, thus the

chemical complexity is expected to be slightly higher, and the electronic effects may be more noticeable.

The HEA-3Cu films were co-sputtered using 50 mm diameter equiatomic quaternary  $\text{Ni}_{25}\text{Fe}_{25}\text{Co}_{25}\text{Cr}_{25}$  and equiatomic quinary  $\text{Ni}_{20}\text{Fe}_{20}\text{Co}_{20}\text{Cr}_{20}\text{Cu}_{20}$  sputtering targets, powered with radio frequency power supplies at 200 and 30 W, respectively. The HEA-20Cu films were sputter-deposited with the equiatomic quinary target at 200 W of DC power. The deposition process has been described previously [45]. A thin HEA-20Cu film with a thickness of  $\sim 70$  nm was deposited directly onto NaCl substrates to ease sample preparation for thermal annealing and ion irradiation experiments within a transmission electron microscope [40,45]. During the sputtering, no intentional substrate heating was applied. Films with columnar structure grown perpendicular to the wafer surface were observed. The average grain size was up to a few tens of nanometers, as determined by cross-sectional TEM and XRD.

### 2.2. Thermal annealing and sequential irradiation within an electron microscope

In-situ thermal annealing and in-situ irradiation were both carried out within a Hitachi H-9500 TEM at temperatures up to 773 K for 30 min using the MIAMI-2 system at University of Huddersfield [40,68]. The microscope, equipped with a Gatan double-tilt heating holder, was operated at 300 kV. The thin HEA-20Cu films were uniformly irradiated with 134 keV  $\text{Xe}^+$  ions with a flux of  $5.5 \times 10^{12} \text{ cm}^{-2}\text{s}^{-1}$  at the temperatures of 273, 573 and 773 K, respectively. For the relatively low  $\text{Xe}^+$  ion energy used here, grain growth is mainly driven by collision cascades where elastic thermal spikes dominate.

### 2.3. Ion irradiation, recoil spectra and associated energy deposition

High-energy Ni (3, 11, and 23 MeV) and Au (11 and 23 MeV) ions to various fluences were used to evaluate the microstructural responses to different levels of ionizing energy ( $E_{\text{ionization}}$ , the energy loss to electrons) and damage energy ( $E_{\text{damage}}$ , the energy to create recoils) depositions [51,69], as well as different ratios between the two (see Table 1). While a higher energy of the Au beam (e.g., 100 MeV) may be more desirable, 23 MeV is close to the maximum achievable energy with sufficient beam current from the accelerator at the University of Tennessee used for these irradiation studies [70]. The irradiations were performed perpendicular to the sample surface. To ensure uniform irradiation, the ion beam was defocused and wobbled over the sample surface during the irradiation with horizontal and vertical scan frequencies of 517 and 64 Hz, respectively [70]. The ion flux, included in Table 1, was chosen to avoid notable beam heating, but was still sufficient to reach the desired dose within a reasonable time. All the irradiations were carried out at room temperature to further minimize thermally induced defect migration and to better understand radiation-induced athermal effects [51].

The Stopping and Range of Ions in Matter (SRIM) code with the option of Detailed Calculation with Full Damage Cascades [51,69,71] was used to estimate the average dose in the film and the energy deposition to both the atomic and electronic subsystems along the surface normal. The simulations assumed a single composition over a depth beyond 1.0  $\mu\text{m}$ , rather than representing energy deposition and damage to the silicon (Si) substrate, which are irrelevant to the current study. Densities of  $8.236 \text{ g cm}^{-3}$  ( $8.766 \times 10^{22} \text{ atoms cm}^{-3}$ ) and  $8.356 \text{ g cm}^{-3}$  ( $8.705 \times 10^{22} \text{ atoms cm}^{-3}$ ) were used in the SRIM calculations for HEA-3Cu and HEA-20Cu films, respectively. A threshold displacement energy of 40 eV was used for all the elements. The atomic displacement profile (Fig. 1) based on full-cascade simulations [51,69] is the sum of the vacancies from all target elements plus the replacement collisions. The equivalent damage doses in dpa for a Ni or Au ion fluence of  $10^{14} \text{ cm}^{-2}$  are shown by the dashed lines in Fig. 1. For the MeV ions used in this study, a significant fraction of the implanted Ni or Au ions penetrated the HEA films and were deposited in the Si substrate (not shown). The

**Table 1**

Ion irradiation conditions, together with SRIM-predicted damage dose at 500 nm (for a fluence of  $1 \times 10^{14} \text{ cm}^{-2}$ ). Also included are integrated damage energy ( $E_{\text{damage}}$ ) and integrated total ionization energy ( $E_{\text{ionization}}$ ) per ion over the film thickness (1  $\mu\text{m}$ ), along with the ratio of ionization to damage energy deposition ( $E_{\text{ionization}}/E_{\text{damage}}$ ) and total integrated ion energy deposition ( $E_{\text{total}}$ ) per ion in the film.

Ion and HEA film	$E_{\text{irr}}$ (MeV)	Flux ( $\times 10^{12} \text{ cm}^{-2}\text{s}^{-1}$ )	Max Fluence ( $\times 10^{14} \text{ cm}^{-2}$ )	Dose (dpa)	$E_{\text{damage}}$ (keV)	$E_{\text{ionization}}$ (keV)	$E_{\text{ionization}}/E_{\text{damage}}$	$E_{\text{total}}$ (keV)
Ni in HEA-3Cu	3	5.3–6.7	2365	0.14	694	1852	2.7	2546
Ni in HEA-3Cu	11	3.0	800	0.041	193	5607	29	5800
Ni in HEA-3Cu	23	0.83–0.85	499	0.020	100	11,376	113	11,476
Ni in HEA-20Cu	3	6.94	800	0.15	706	1804	2.6	2510
Au in HEA-20Cu	11	3.3–3.4	598	0.62	2693	6243	2.3	8935
Au in HEA-20Cu	23	0.14	79	0.29	1267	7713	6.1	8979

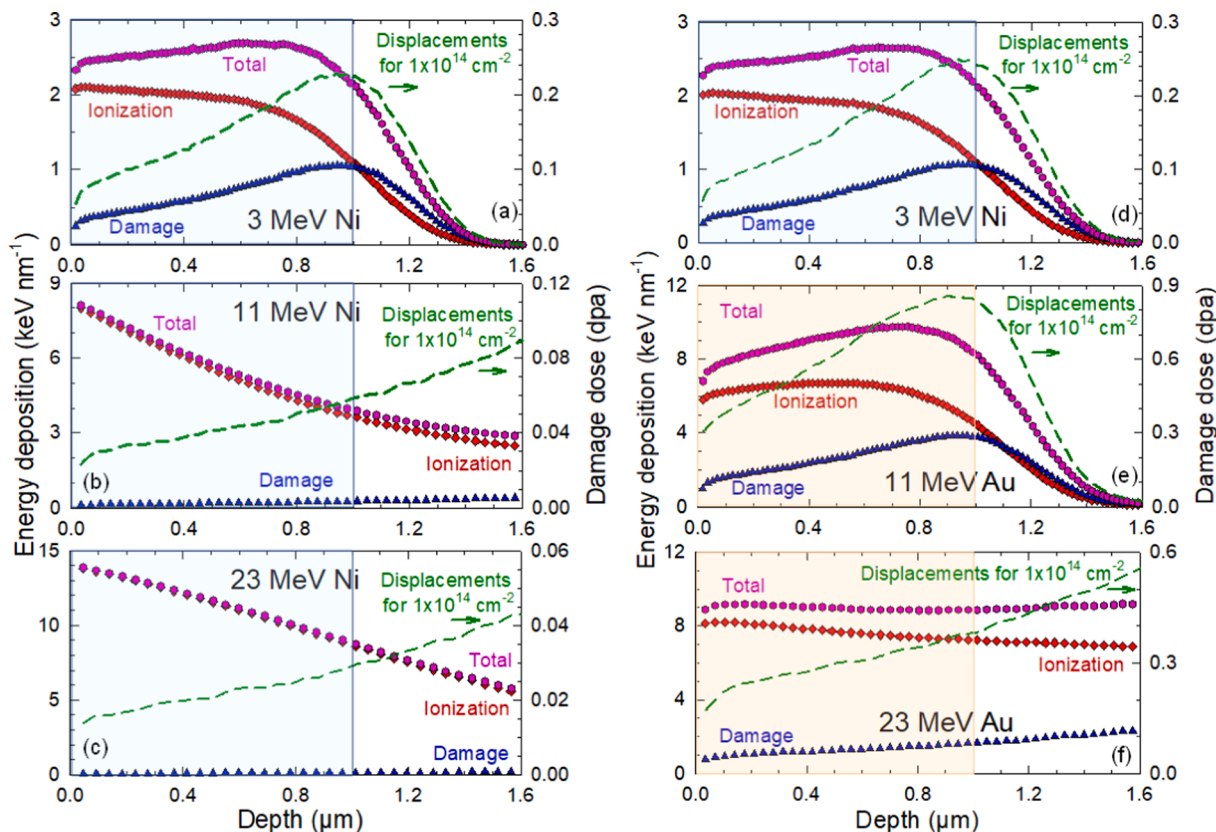


**Fig. 1.** SRIM-predicted average energy deposition per unit of depth from one ion along the surface normal (left axis) and equivalent damage dose profile for an ion fluence of  $1 \times 10^{14} \text{ cm}^{-2}$  (right axis) in HEA-3Cu (left column) and HEA-20Cu (right column), respectively, for (a) 3 MeV Ni, (b) 11 MeV Ni, and (c) 23 MeV Ni in HEA-3Cu; and for (d) 3 MeV Ni, (e) 11 MeV Au and (f) 23 MeV Au in HEA-20Cu. Damage energy is the energy deposited to produce displacements during collision cascades, ionization is the total energy transferred to target electrons from both ions and recoils, and total energy is the sum of energy deposition to both electronic and atomic subsystems. The shaded areas show the actual film thickness; light blue and orange colors indicate Ni or Au ion irradiation, respectively, for easy visual separation. (For interpretation of the references to colour in this figure legend, the reader is referred to the web version of this article.)

highest fluences for the different irradiation conditions are given in Table 1.

For 3 MeV Ni in HEA-3Cu at the highest fluence of  $2.365 \times 10^{17} \text{ cm}^{-2}$  (Table 1), the estimated concentration of injected Ni ions is 0.45% at a depth of 500 nm, which is an insignificant composition change. The next-highest fluence is  $8.0 \times 10^{16} \text{ cm}^{-2}$  for 3 MeV Ni in both HEA-3Cu and HEA-20Cu, and for 11 MeV Ni in HEA-3Cu. The corresponding concentration of injected Ni at 500 nm decreases by  $\sim 1/3$  for the 3 MeV Ni irradiation and decreases even more for the 11 MeV Ni irradiation. Thus, compositional changes in all the irradiated HEA films were negligible.

In addition to the ion irradiation-related parameters, the SRIM-predicted values of deposited energies integrated over the 1  $\mu\text{m}$  film and energy profiles along surface normal are listed in Table 1 and shown in Fig. 1, respectively. The dose values for each ion-alloy combination corresponding to an ion fluence of  $1 \times 10^{14} \text{ cm}^{-2}$  are based on SRIM full-

cascade predictions at a depth of 500 nm. The term  $E_{\text{irr}}$  is the ion energy impinging on the surface of the HEA films. Energy loss to the target electronic system ( $E_{\text{ionization}}$ ) is the sum of ionization losses by both ions and recoils. As noted previously [51], energetic recoils can further excite target electrons and induce cascade damage; and their kinetic energy will transfer to both target atoms and electrons, which are consequently differentiated into damage energy or ionization energy. Accordingly,  $E_{\text{ionization}}$  is defined as the total electronic energy transfer to target electrons from both ions and energetic recoils. The damage energy ( $E_{\text{damage}}$ ), calculated as described elsewhere [51,69,72], is the energy consumed to form atomic displacements. The total energy deposition ( $E_{\text{total}}$ ) is therefore defined as  $E_{\text{ionization}} + E_{\text{damage}}$ . It is not surprising that  $E_{\text{damage}}$  and the damage dose profile have a similar depth dependence, as they describe the same physical process [69,72]. We note that these energies ( $E_{\text{ionization}}$ ,  $E_{\text{damage}}$ , and  $E_{\text{total}}$ ) are used below in two different ways: the projected energy loss per unit of depth with units of keV/nm,

and the integrated energy deposited over 1  $\mu\text{m}$  depth of the film with units of keV.

Pysrim is a python library for automating SRIM calculations, for analysis and for producing quality plots [73]. To further assess the impact of  $E_{\text{ionization}}$  and  $E_{\text{damage}}$  on microstructural evolution, Pysrim was used to determine the recoil spectra and radial distribution of full-cascade events.

#### 2.4. Characterization of as-deposited and irradiated films using complementary techniques

The structural stability, crystallite growth, and possible elemental segregation of the as-deposited and irradiated HEA films were characterized by scanning electron microscopy (SEM), scanning transmission electron microscopy (STEM), cross-sectional TEM, selected-area electron diffraction (SAED), and XRD. Energy-dispersive x-ray spectroscopy (EDS) was used in conjunction with SEM and STEM to determine the elemental composition of the entire HEA films. SEM images and EDS mappings were taken on a FEI Versa 3D dual beam focused ion beam/scanning electron microscope (FIB/SEM) equipped with an Oxford Instruments silicon drift detector EDS system. TEM images were taken at different conditions: at focus and under focus, and in both bright-field (BF) and dark-field (DF) modes. STEM images for these as-deposited and irradiated samples were taken in BF, low-angle annular dark field (LAADF), medium-angle annular dark field (MAADF), and high-angle annular dark field (HAADF) modes having 9, 12–20, and 61–200 mrad collection angles, respectively, for a probe convergence angle of 7.5 mrad. DF images have enhanced contrast compared with the BF images, specifically when imaging nanocrystalline features.

TEM/STEM imaging was conducted at Oak Ridge National Laboratory using a FEI Talos 200 keV S/TEM equipped with an X/field emission gun (FEG) high-brightness field emission source, BF and multiple ADF detectors, and a quadrupole FEI ChemiSTEM EDS collection system. Some HEA-20Cu specimens were prepared by an FIB lift-out technique using an FEI Helios Nanolab Dual beam workstation at the University of Michigan [47]. A flash polishing technique [45,74] was applied to remove FIB damage before conducting cross-sectional TEM and STEM characterization. A double Cs-corrected JEOL 3100R05 STEM microscope at Michigan was operated at 300 keV to take BF and HAADF images.

Irradiation-induced growth of crystallites was characterized using XRD. A D2 Phaser, Bruker Inc., Benchtop x-ray diffractometer with a maximum operating tube power of 0.3 kW (30 kV and 10 mA) and Cu K $\alpha$  radiation was used. All the XRD patterns were collected using a 0.004 step size and in a 10–110° 2 $\theta$  range over an ~ 10 h acquisition time. Rietveld analysis was applied to fit the experimental XRD patterns using GSAS software [75]. Anomalies in the backgrounds of some XRD patterns were removed using OriginPro software before peak fitting. Both Williamson – Hall (W – H) relationship [45] and the Scherrer equation were applied to determine crystallite sizes and to show the trend of the irradiation-induced response of the samples. The W – H plot is described as  $\beta_t \cdot \cos\theta = K \cdot \lambda / \tau + 4\epsilon \cdot \sin\theta$ , where  $\epsilon$  is the microstrain (irrelevant to the focus in the current study and not reported here). In the W – H method, the intercept and slope of a plot of  $\beta_t \cdot \cos\theta$  versus  $\sin\theta$  were used to determine the crystallite size and microstrain of the samples, respectively. If peak intensities, especially of high-angle peaks, were weak, the Scherrer equation was used in obtaining crystallite sizes using individual peaks with sufficient intensity at low angles, such as the main diffraction (111) peak. The Scherrer equation is described as  $\tau = K \cdot \lambda / (\beta_t \cdot \cos\theta)$ , where  $\tau$  is the crystallite size,  $K$  is the shape factor (0.94 for spherical crystallites is assumed),  $\lambda$  is the wavelength,  $\theta$  is the diffraction angle in radians, and  $\beta_t$  is the peak broadening. A National Institute of Standards and Technology Si-SRM640D internal standard was used to correct any sample displacement occurring during XRD pattern acquisition and to determine the instrumental peak broadening. The peak broadening was determined by correcting the instrumental peak broadening using  $\beta_t^2 =$

$\beta_{\text{obs}}^2 - \beta_{\text{ins}}^2$ , where  $\beta_{\text{obs}}$  and  $\beta_{\text{ins}}$  were the observed and instrumental peak broadening, respectively. The one standard deviations ( $\sigma$ ) of the mean values of the crystallite sizes determined using the Scherrer equation were reported in this study. No error value was given for the crystallite sizes determined using the W – H method, since only one set of data was used in each sample and no other technique was used to compare with these data. Note that the XRD results represent an average size of the coherently diffracting crystallites and may not be the same as the grain size measured by TEM.

### 3. Results and discussion

Ions lose energy along their trajectories by transferring kinetic energy to atomic nuclei, inducing atomic displacements and elastic thermal spikes, and to target electrons, creating hot electrons and inelastic thermal spikes [51]. This study focuses on ionization effects in complex alloys, rather than the irradiation performance of HEAs. To demonstrate that electronic energy dissipation induces instabilities at GBs and highlight that irradiation-induced grain growth is attributed to more than atomic displacements during the collision cascades (i.e.,  $E_{\text{damage}}$  deposition), Ni and Au at different energies are chosen to deposit comparable  $E_{\text{damage}}$  and  $E_{\text{ionization}}$  or dominant  $E_{\text{ionization}}$  in the HEA films. The depth-dependent energy partitioning of MeV Ni and Au ions in HEA-3Cu and HEA-20Cu is shown in Fig. 1, left and right columns, respectively. The integrated  $E_{\text{damage}}$  and  $E_{\text{ionization}}$  deposited per ion over the thicknesses of the 1  $\mu\text{m}$  films are summarized in Table 1. As noted,  $E_{\text{damage}}$  and  $E_{\text{ionization}}$  are the total energy transfer from one ion to target nuclei, producing atomic displacements (i.e., elastic thermal spikes), and to electrons, causing ionization and subsequent inelastic thermal spikes, respectively. Both the average damage dose for a fluence of  $1 \times 10^{14} \text{ cm}^{-2}$  and the ratio of  $E_{\text{ionization}}/E_{\text{damage}}$  are also included in Table 1. Comparable energy deposition and damage dose profiles (shown in Fig. 1a and d) and values (in Table 1) for 3 MeV Ni in HEA-3Cu and HEA-20Cu are attributed to the similar mass of the alloying elements and the film densities, even though the composition of the two films is different.

As revealed in Table 1 for the energy deposition in both HEA-3Cu and HEA-20Cu, there are large variations in integrated  $E_{\text{damage}}$  and  $E_{\text{ionization}}$ , ranging from 100 to 2693 keV and from 1804 to 11376 keV, respectively. Moreover, the variation of the  $E_{\text{ionization}}/E_{\text{damage}}$  ratio is also significant, from 2.3 to 113. The difference of the  $E_{\text{ionization}}/E_{\text{damage}}$  ratio is large in the HEA-3Cu film under Ni irradiation, from 2.7 to 113, which is designed to reveal the impact of ionization (Sect. 3.1). The change of the  $E_{\text{ionization}}/E_{\text{damage}}$  ratio is evident but not significant in HEA-20Cu films, ranging from 2.3 to 6.1; nonetheless, the large difference in ion mass between Ni and Au ions makes it suitable to study the impact of energy partitioning (Sect. 3.2) and influence of recoil spectra (Sect. 3.3). While a more clearer ionization effect is expected for high-energy Au ions (such as at 150 MeV, in which the  $E_{\text{ionization}}/E_{\text{damage}}$  ratio is close to 110, approaching a similar level as 23 MeV Ni ions shown in Table 1) with higher  $E_{\text{ionization}}/E_{\text{damage}}$  ratio than in the current study, the energies in the present study (Table 1) cover the more common irradiation conditions used for irradiation studies. Since the damage profile is essentially the same as the dpa profile, irradiation-induced growth of crystallites in HEA-3Cu and HEA-20Cu is evaluated as a function of increasing  $E_{\text{damage}}$  and  $E_{\text{total}}$ , respectively.

#### 3.1. Growth of crystallites in HEA-3Cu under ion irradiation with large changes in $E_{\text{ionization}}/E_{\text{damage}}$ ratio: impact of ionization

To evaluate the impacts of electronic and atomic processes on ion-induced grain growth, Ni irradiations at different energies were performed on nanocrystalline HEA-3Cu films. In these irradiated HEA-3Cu films, the  $E_{\text{ionization}}/E_{\text{damage}}$  ratio increases from 2.7 to 29 and 113 as the Ni energy increases from 3 MeV to 11 and 23 MeV, respectively. As shown in Fig. 1a, neither  $E_{\text{damage}}$  nor  $E_{\text{ionization}}$  is negligible in the case of 3 MeV Ni irradiation. For 11 and 23 MeV Ni in HEA-3Cu (in the shaded

area in Fig. 1b and c), the high ratios of  $E_{\text{ionization}}$  to  $E_{\text{damage}}$  of 29 and 113, respectively, suggest that damage energy is less significant. The near-negligible  $E_{\text{damage}}$  is reflected by the small difference between the total energy deposition by incident ions ( $E_{\text{total}}$ ) and the ionization energy ( $E_{\text{ionization}}$ ) in the films, noting that the thickness of the HEA-3Cu films is about one micrometer. The average dose values and damage energies deposited are related as mentioned previously, since both parameters describe the same physical phenomena: atomic displacements and the energy consumed to produce such displacements, respectively. For 3, 11, and 23 MeV Ni in HEA-3Cu, the large variation in  $E_{\text{ionization}}/E_{\text{damage}}$  ratios can significantly affect the microstructural response of HEA-3Cu, and the effect of  $E_{\text{ionization}}$  or  $E_{\text{total}}$  ( $=E_{\text{damage}} + E_{\text{ionization}}$ ) should be evaluated.

The as-deposited HEA-3Cu film was characterized using complementary techniques. As shown by the STEM and STEM-EDS images in Fig. S1, columnar grains with diameters of  $\sim 20$  nm are clearly visible, and the film is homogeneous. To further investigate the phase stability and evolution of microstructural change under ion irradiation with better statistics, XRD was carried out to examine the growth of

crystallites over a much larger area (i.e., a larger number of grains). The results show that the fcc phase is stable under irradiation as expected [45]. The crystallite sizes determined using both the W – H plot and the Scherrer equation are summarized in Fig. 2 as a function of integrated  $E_{\text{damage}}$ ,  $E_{\text{ionization}}$  and  $E_{\text{total}}$ ; and the R-squared ( $r^2$ ) value [76] is marked at the right bottom corner of each plot. For the 3 MeV Ni irradiation, only one data point ( $3.0 \times 10^{15} \text{ cm}^{-2}$ ) is included in the W – H plot shown in the left column because high-angle peaks from other irradiated samples at higher fluences are not clearly visible from the background. More data points determined from individual peaks are available in the right column of Fig. 2, corresponding to the reflections for the fcc crystallography of the samples using the Scherrer formula.

To evaluate if the microstructural instability results mainly from direct displacement collisions ( $E_{\text{damage}}$ ) and if the contribution from ion energy transfer to electrons ( $E_{\text{ionization}}$ ) is negligible, irradiation-induced growth as a function of integrated  $E_{\text{damage}}$ ,  $E_{\text{ionization}}$  and  $E_{\text{total}}$  in the HEA-3Cu films is compared in Fig. 2. Noteworthy clustering of the data points is observed when the crystallite size is plotted as a function of integrated  $E_{\text{ionization}}$  (Fig. 2b and e) or integrated  $E_{\text{total}}$  (Fig. 2c and f), as

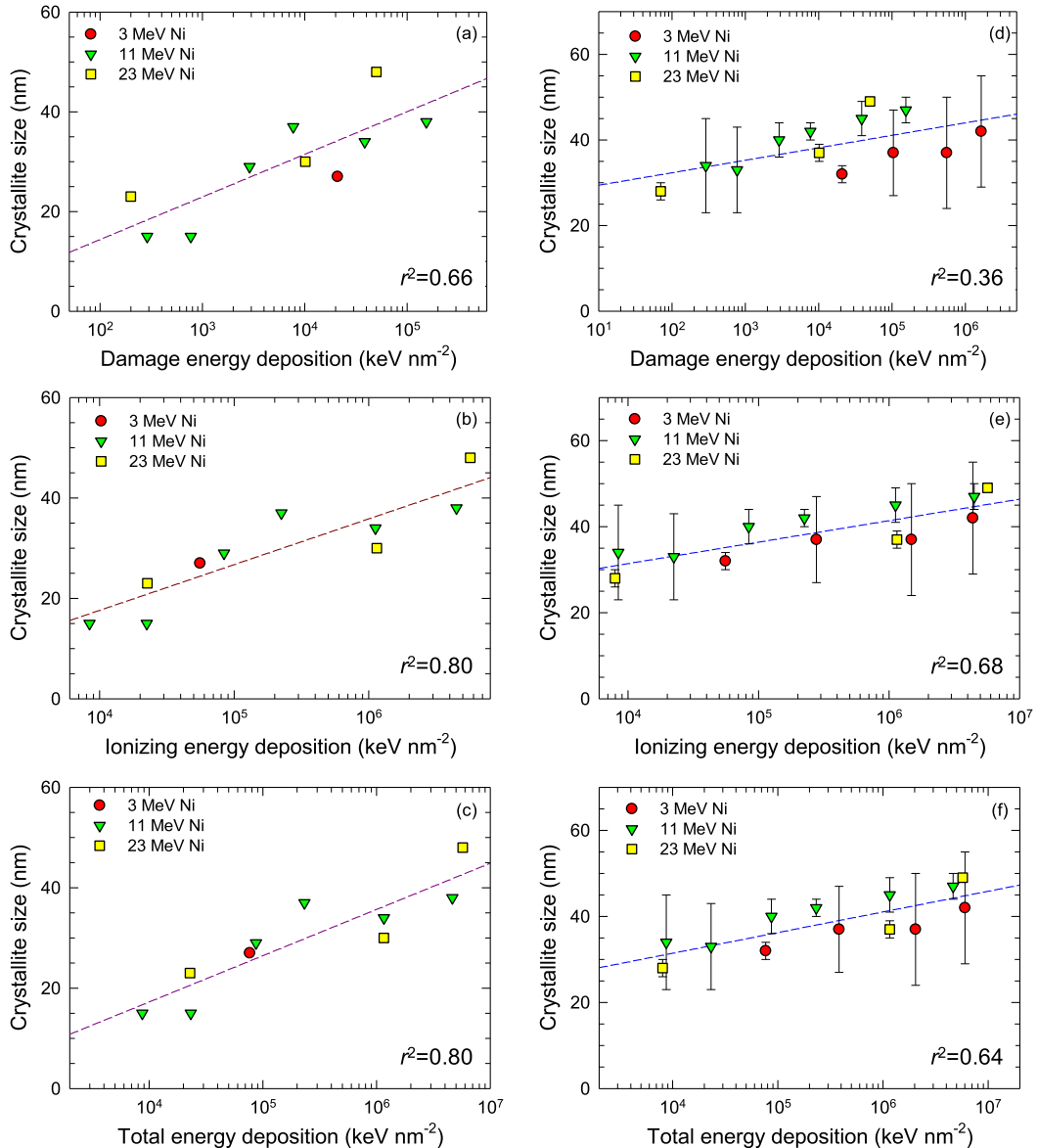


**Fig. 2.** Ni irradiation-induced growth of crystallites in HEA-3Cu film determined using the W – H method (left: a, b, and c) and Scherrer formula from the (111) diffraction peak (right: d, e and f). The estimated crystallite size is plotted as a function of  $E_{\text{damage}}$  (a and d),  $E_{\text{ionization}}$  (b and e) and  $E_{\text{total}}$  (c and f). The dashed lines are the linear regression. The coefficient of determination ( $r^2$ ) is the square of the correlation.

is clearly reflected by the increase in  $r^2$  from 0.66 to 0.80, based on the W – H approach, and from  $\sim 0.36$  to  $\sim 0.64$  and 0.68 by fitting to the Scherrer equation. In general, weak or low dependence (i.e., the coefficient of determination) is regarded for  $0.3 < r^2 < 0.5$ , moderate dependence for  $0.5 < r^2 < 0.7$ , and strong dependence for  $r^2 > 0.7$ , respectively [76]. Based on the W – H approach (Fig. 2, left), the increase in  $r^2$  from 0.66 to 0.8 shows that the correlation changes from moderate to strong when the contribution of  $E_{\text{ionization}}$  is considered (Fig. 2b) and included (Fig. 2c). Similarly, the correlation changes from weak ( $r^2 = 0.36$ ) to moderate ( $r^2 = 0.68$  or 0.64) based on the Scherrer approach (Fig. 2, right). The similar energy dependence and  $r^2$  values, observed in Fig. 2b and c or in Fig. 2e and f, are attributed to the dominant contribution of  $E_{\text{ionization}}$  in  $E_{\text{total}}$  (Table 1 and Fig. 1b and c).

The notable clustering of the data points in Fig. 2 when  $E_{\text{ionization}}$  is considered suggests that energy transfer to target electrons has a significant impact on microstructural evolution and leads to effective grain growth. Given the small and dominant contributions of  $E_{\text{damage}}$  and  $E_{\text{ionization}}$  in  $E_{\text{total}}$ , respectively, under 11 and 23 MeV Ni irradiations, the results in Fig. 2 suggest that the damage energy from elastic collision is more effective in inducing microstructure instability. It is, however, also clear that the contribution from ion energy transfer to electrons cannot be ignored and studying such coupled energy dependences ( $E_{\text{damage}}$  and  $E_{\text{ionization}}$ ) should provide insights into the ion–solid interaction processes [51].

### 3.2. Growth of crystallites in HEA-20Cu under ion irradiation with small changes in $E_{\text{ionization}}/E_{\text{damage}}$ ratio: Impact of energy partitioning

The microstructural response to ion energy deposition is further investigated using the HEA-20Cu film. In an effort to better understand and even to quantify the contributions of integrated  $E_{\text{damage}}$  and  $E_{\text{ionization}}$ , 3 MeV Ni and 11 MeV and 23 MeV Au ions were used, as they deposit significant energy to both electronic and atomic structures but with somewhat comparable  $E_{\text{ionization}}/E_{\text{damage}}$  ratio. As shown in the right column of Fig. 1 and the bottom half of Table 1, neither  $E_{\text{damage}}$  nor  $E_{\text{ionization}}$  is negligible, and the  $E_{\text{ionization}}/E_{\text{damage}}$  ratio ranges from 2.3 for 11 MeV Au ions to 2.6 and 6.1 for 3 MeV Ni and 23 MeV Au ions, respectively.

Five as-deposited HEA-20Cu samples cut randomly from the as-deposited wafer were examined by XRD; their crystallite size ranges between 13 and 14 nm, with an average value of 13.8 nm determined by the W – H plot. Applying the Scherrer equation, the crystallite size ranges from 28 to 32 nm with an average of 30.8 nm.

The cross-sectional TEM image in Fig. S2a shows columnar grains with smaller diameters near the interface and grains with larger diameters close to the surface. Two high-magnification TEM images taken at  $\sim 300$  and 500 nm from the surface are included to show the grain structure. A TEM image of a 3 MeV Ni sample irradiated to  $1.5 \times 10^{16} \text{ cm}^{-2}$  (23 dpa) is shown in Fig. S2b. Compared with the as-deposited film (Fig. S2a), notable irradiation-induced growth is evident, reflected by the contrast between different columnar grains. Such grain growth is also supported by the corresponding SAED patterns, which indicate more discrete diffraction spots after irradiation.

The composition uniformity of the HEA-20Cu films before and after irradiation is also examined. Figure S3a (the first columns to the left) show SEM-EDS images of the as-deposited film showing the uniform elemental distribution of the as-deposited films. STEM-BF, LAADF, MAADF, and HAADF images of the HEA-20Cu film on a SiO<sub>2</sub>/Si substrate after room temperature irradiation to  $5.98 \times 10^{16} \text{ cm}^{-2}$  (372 dpa) using 11 MeV Au ions are shown in Figs. S3b-e, together with the EDS maps. As mentioned earlier, the objective of this work is to reveal ionization effects, the other aspects of irradiation responses and mechanical performance will be the subject of future studies. The STEM and EDS images in Fig. S3 confirm that the HEA-20Cu film is well intact. Moreover, the STEM images (Figs. S3b-e) show the growth of grains with an average width of  $\sim 61$  nm from the as-deposited film of  $\sim 30.8$

(Fig. S2a).

Fig. 3 presents the grain growth as a function of integrated  $E_{\text{damage}}$  and  $E_{\text{total}}$ . Due to the insignificant difference in the  $E_{\text{ionization}}/E_{\text{damage}}$  ratio in the HEA-20Cu films, compared with the Ni irradiation results for HEA-3Cu films shown in Table 1 and Fig. 2, grain growth is not plotted or analyzed as a function of  $E_{\text{ionization}}$  in Fig. 3. Although irradiation-induced crystallite growth is observed from both the W – H plot (Fig. 3 left) and the Scherrer equation (Fig. 3 right), the clustering of data points when the contribution of integrated  $E_{\text{ionization}}$  is included is not as strong as in the case of Ni-irradiated HEA-3Cu. Insignificant clustering—seen as the similar  $r^2$  values from 0.80 to 0.85 in Fig. 3 left, and from 0.70 to 0.76 in Fig. 3 right—is attributable to the difference in recoil spectra (discussed below) and the insignificant change of the  $E_{\text{ionization}}/E_{\text{damage}}$  ratio in HEA-20Cu from 2.3 to 6.1 (see Table 1 and Fig. 1 right). This case is significantly different from the HEA-3Cu case having the large ratio changes from 2.7 to 113 and the dominant contribution of  $E_{\text{ionization}}$  under 11 MeV and 23 MeV Ni ion irradiation (Table 1 and Fig. 1 left).

When the variation of  $E_{\text{ionization}}/E_{\text{damage}}$  ratio is small and both energy deposition processes (i.e.,  $E_{\text{ionization}}$  and  $E_{\text{damage}}$ ) contribute to the grain growth, the irradiation response of HEA-20Cu films suggests that the impact of energy partitioning is difficult to delineate or quantify for a HEA system with insignificant chemical complexity, as the one studied here. Nevertheless, more smooth growth dependence is observed under Ni ion irradiation, as compared with Au ion irradiation, which motivates us to pay attention to the intrinsically spatially and temporally coupled nuclear and electronic energy dissipation processes.

### 3.3. Coupled electronic and atomic energy dissipation

Ion–solid interaction induces localized processes at far-from-equilibrium conditions. The passage of an MeV ion through HEAs causes a strong local intrusion that produces a large number of vacancies and interstitials within a short timescale (fractions of a picosecond) [77] and mostly within a small radius of the ion trajectory. Collision cascades coupled with inelastic thermal spikes can be viewed as an ultra-fast, nanoscale phase transition with complex thermodynamic and kinetic behavior [51]. Since the energy transferred from an ion to an atomic nucleus in a single collision is often many times greater than the binding energy of a few eV, the atom can be displaced from its original site in the lattice. Primary knock-on atoms may receive sufficient energy that they in turn can displace other atoms (i.e., secondary recoils), creating a cascade of atomic collision events that dissipate  $E_{\text{damage}}$  to phonons. During the cascade and sub-cascade events, extreme transient pressures and temperatures can occur from high-energy recoils (Fig. 4), as revealed by atomistic simulations of recoils with energies of tens of keV [78]. For example, a typical 10 keV collision cascade in Ni can create a supersonic shockwave involving pressures of 10–50 GPa and temperatures of several thousands of Kelvin as the shockwave transitions to a sonic velocity [78]. Eventually, many atoms can be set in motion, with energy dissipated through phonons as a rapid quenched elastic thermal spike [51].

Besides elastic thermal spikes induced by PKAs, additional energy loss to electrons leads to additional localized electronic excitations and local lattice heating [51]. The significant transfer of energy from incident ions to the electronic structure (Fig. 1 and Table 1) creates energetic electrons that produce a cascade of electron collisions in the electronic structure along the ion path (i.e., an inelastic thermal spike). Such processes are described by Ulmer and Motta [79] as an “instantaneous line-source of heat” that diffuses radially outward along the ion path, which is accounted for in a rate theory model to explain microstructural evolution observed in ZrC at cryogenic temperatures.

The response of materials to ion energy deposition is inherently connected with a simultaneous disturbance of the electronic and atomic structures. The coupled electronic and nuclear energy dissipation and subsequent nonequilibrium processes in materials are important aspects

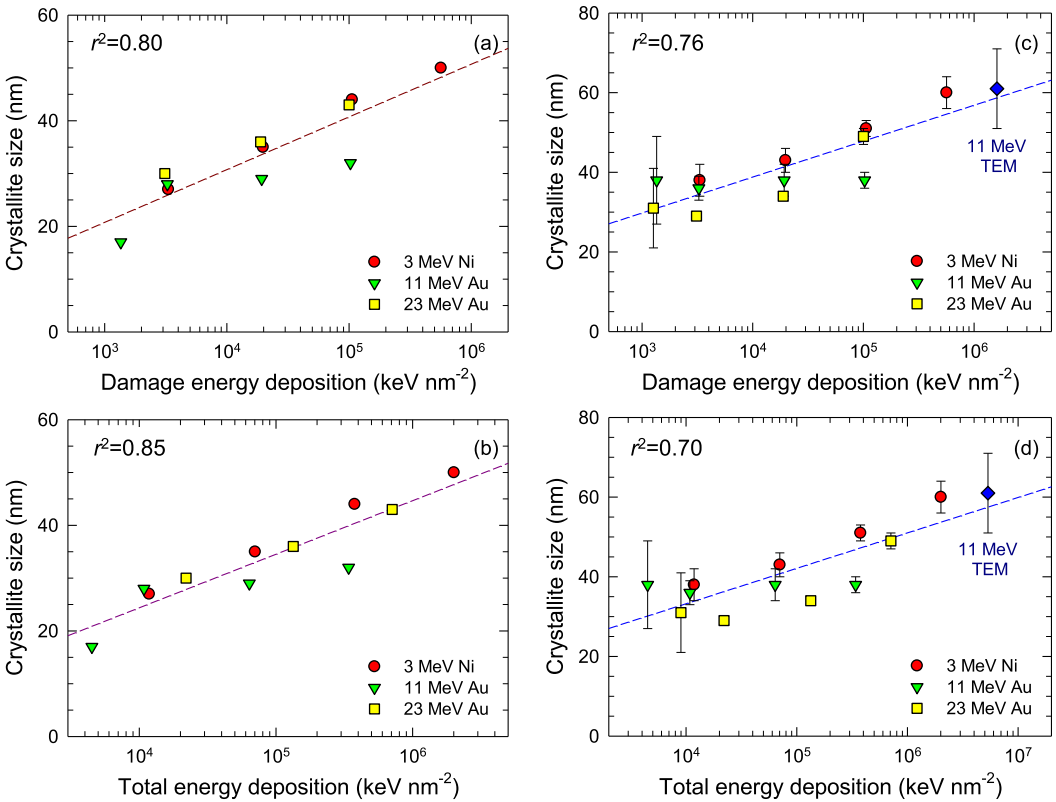


**Fig. 3.** Crystallite size in the HEA-20Cu film, determined using the W – H method (left: a and b) and Scherrer formula from the (111) diffraction peak (right: c and d). The estimated crystallite size is plotted as a function of  $E_{\text{damage}}$  and  $E_{\text{total}}$ . The dashed lines are the linear regression. Also included in the plots on the right is the grain size determined from TEM images after 11 MeV Au irradiation to  $5.98 \times 10^{16} \text{ cm}^{-2}$ . The coefficient of determination ( $r^2$ ) is the square of the correlation.

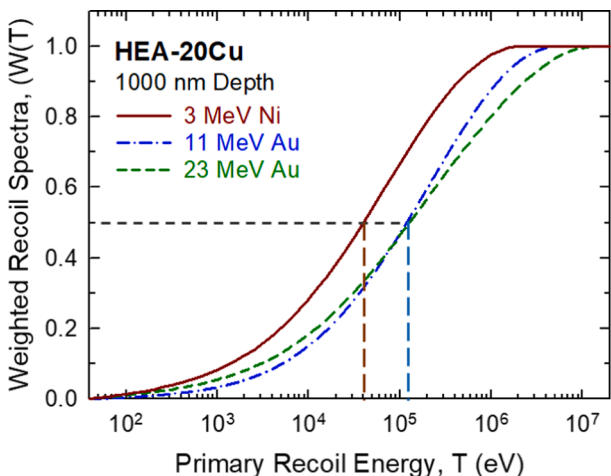


**Fig. 4.** The weighted recoil spectrum for Ni and Au ions within the first micrometer in the HEA-20Cu film. The long-dashed lines indicate the PKA energy below which  $\sim 50\%$  of the displaced atoms are produced.

in understanding and predicting how materials may respond to external energy deposition. Radiation-induced grain growth has previously been attributed to elastic spikes (i.e., displacements during collision cascades) [80–85], but more recent work has revealed that grain growth can be attributed to both  $E_{\text{ionization}}$  and  $E_{\text{damage}}$  in nanocrystalline oxides [51,55]. In nanocrystalline  $\text{CeO}_2$  and  $\text{ZrO}_2$  [55], the irradiation-induced grain growth under both Si and Au irradiation is attributed to  $E_{\text{total}}$ , in which both  $E_{\text{damage}}$  and  $E_{\text{ionization}}$  contribute additively to the overall grain growth. The importance of the coupled effects has been reviewed for other materials [51]. In a study of coupled electronic and atomic

effects on defect evolution in SiC under ion irradiation [86], temporal and spatial coupling of energy dissipation in electronic and atomic subsystems is evaluated in SiC under MeV irradiation with different ions (ranging from C to Au). The results show that both  $E_{\text{ionization}}$  and  $E_{\text{damage}}$  induce transient instabilities, and the strong temporal and spatial coupling of ionization with displacement events suppresses in-cascade defect production and anneals preexisting damage.

The strong coupling of ionization with displacement events discovered in nanocrystalline oxides and carbides may not be negligible in complex alloys where the electron–phonon ( $e\text{-}ph$ ) coupling is much stronger and ion energy dissipates much slower via electrons. In HEAs and many other CSAs, high electronic temperatures result in highly localized inelastic thermal spikes on the atomic lattice via  $e\text{-}ph$  coupling that can result in enhanced atomic mobility [87], phase transformation [47], formation [88] or annihilation [32] of atomic-scale defects, and can drive local structures far from equilibrium [51,78]. Most of the energy transferred to electrons is dissipated (in less than a ps) in an inelastic thermal spike via  $e\text{-}ph$  coupling [51,89]. The increase in  $e\text{-}ph$  coupling strength and decrease in electrical thermal conductivity [30,32,87–89] result in much higher temperatures in inelastic thermal spikes and slower heat dissipation. Compared with metals and conventional alloys, which have higher electrical thermal conductivity and weaker  $e\text{-}ph$  coupling, the enhanced energy exchange between the atomic and electronic subsystems in CSAs results in a lower total number of defects and smaller defect clusters under irradiation at energies of up to a few tens of MeV [32,87,89]. But it can also lead to defect creation under GeV ion irradiation [88] in CSAs, whereas few defects are formed in pure metals because of rapid heat dissipation.

To better understand the impact of displacement processes, we determined the weighted primary recoil spectrum,  $W(T)$ , and radial distribution of atomic displacements. The weighted primary recoil spectrum, defined as the fraction of displaced atoms produced by all

primary recoils with energies less than that of a given primary recoil energy, is a useful measure of the overall effect of recoil spectrum on defect production [90]. The W(T) is determined using Pysrim and full-cascade SRIM simulations for 1000 ions over the film thickness of 1  $\mu\text{m}$ ; the results are shown in Fig. 4. As the temporal and spatial coupling of ionization with displacement events may play an important role in defect production and evolution, as well as microstructural instability, Pysrim [73] is used to determine the radial distribution of atomic displacements from full-cascade SRIM simulation of ion events in HEA-3Cu and HEA-20Cu. The spatial distributions of displaced atoms for 1000 incident ions, over the depth range from 450 to 550 nm, are shown in Fig. 5 for all six irradiation conditions (Table 1). Similar spatial distributions are observed for 3 MeV Ni ions in HEA-3Cu and HEA-20Cu, owing to the similar masses of the alloying elements and the film density, as reflected in Fig. 1a and d. To evaluate the grain growth induced by different ions, the crystallite size is plotted as a function of ion fluence in Fig. 6 for all irradiation conditions.

The impact from both electronic and atomic processes can be evaluated based on the results in Figs. 1–6. The weighted recoil spectra (Fig. 4) suggest that about 50% of the displacements are produced by PKAs with energies of less than 40 keV for Ni ions and less than 125 keV for Au ions. Clearly, harder recoil spectra (i.e., higher recoil energies) are observed for the Au ions over the film thickness. The relatively softer recoil spectra from the Ni irradiation produce fewer and more isolated simple defects in the cascade events. When the crystallite size is plotted as a function of integrated  $E_{\text{damage}}$  (i.e., the number of displacement events) in Fig. 3a and c, the softer recoil spectra from Ni ions (i.e., more isolated point defects or small defect clusters) may contribute more efficiently to the grain instability than the spectra from Au ions. All the Ni data (red circles) in Fig. 3 appear above the dashed lines, indicating a more effective contribution from the displacements and suggesting the weighted recoil spectra should be considered.

A clearer perspective of the effect of different ions and energies can be obtained from the radial distributions of defect production from PKA

cascades along an incremental depth of ion trajectories, as shown in Fig. 5. In the case of 23 MeV Au irradiation, the weighted recoil spectrum shows the PKAs extends to higher primary recoil energies than the spectrum for 11 MeV Au irradiation. Given the relatively small difference in recoil spectrum (Fig. 4) and large uncertainty of the data (Fig. 3), it is difficult to delineate the impact of the respective of Au recoil spectra on the effectiveness of grain growth. Nevertheless, the coupled energy deposition processes may lead to noticeable difference on ion-induced instability in complex alloys, as clearly revealed in SiC partially due to very localized covalent bonds [86]. While the radial distribution of displaced atoms from 23 MeV Ni ions (Fig. 5) is comparable to the initial crystallite size, the radial displaced atom distributions for all other ions are much larger than the initial crystallite sizes. Comparing the two radial distributions in Fig. 5e and f, displaced atoms are more clustered along the trajectory of 23 MeV Au, which promotes strong spatial coupling of the inelastic thermal spike with atomic displacement processes. The wider radial spread of displaced atoms from 11 MeV Au ions leads to relatively weaker spatial coupling of electronic and atomic displacement processes (i.e., elastic thermal spikes). Temporal and spatial coupling of energy deposition processes from electrons and recoiling atoms control defect production and grain growth. Further research is required to reveal and quantify the correlation between the coupling strength and damage production or structure instability.

While  $E_{\text{damage}}$  and  $E_{\text{ionization}}$  are not negligible in HEA-20Cu, as shown in Fig. 1d–f and Table 1, energy partitioning in irradiated HEA-3Cu is large (Fig. 1a–c and also in Table 1). A considerable reduction in the number and distribution of displaced atoms in HEA-3Cu is observed with increasing Ni ion energy from 3 MeV to 11 MeV (Fig. 5a and b), which agrees well with the significant drop (by nearly 3.5 times) in the predicted average damage dose and the predicted integrated  $E_{\text{damage}}$  from 0.14 to 0.041 dpa and from 694 to 193 keV (Table 1), respectively. Further reduction in the number and distribution of displaced atoms is clear when the Ni ion energy is further increased from 11 MeV to 23 MeV (Fig. 5b and c), as expected with the damage dose and

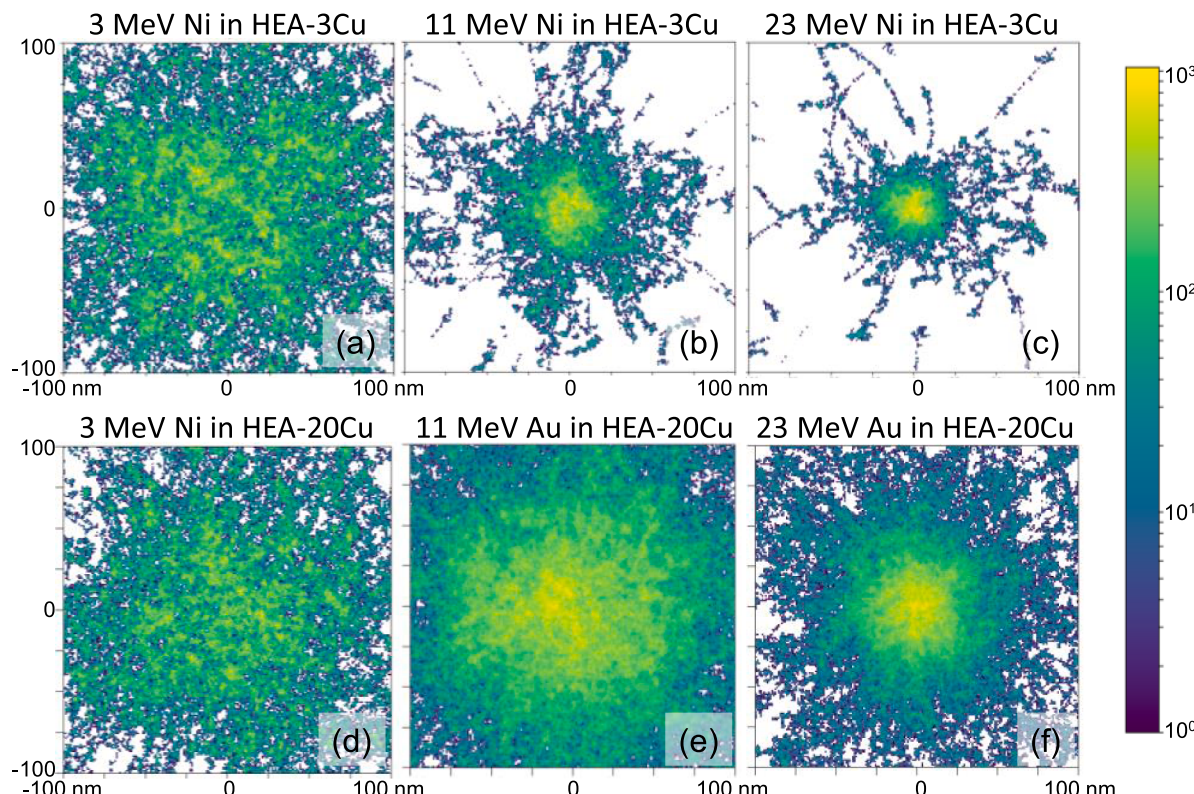


**Fig. 5.** Distribution of displaced atoms from Pysrim based on SRIM full damage cascade simulations for 1000 ions penetrating an HEA-3Cu film (top: a, b, and c) and HEA-20Cu film (bottom: d, e and f) over a depth range of 450 to 550 nm, respectively. The irradiation condition is specified at the top of each plot.

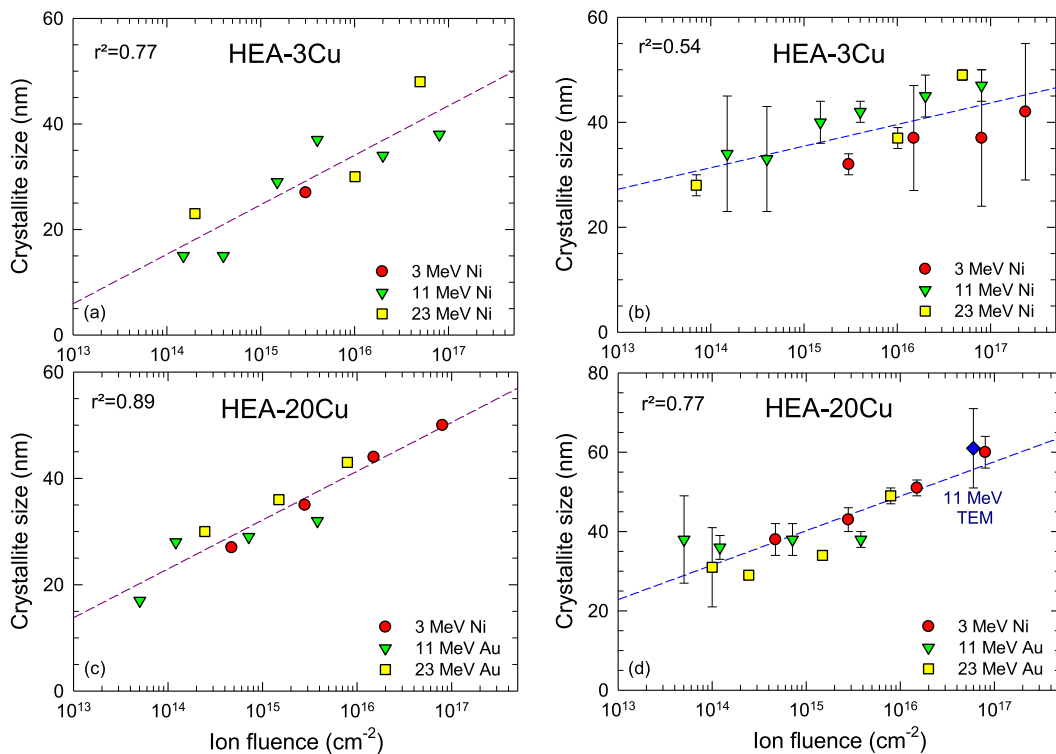


**Fig. 6.** Crystallite size in HEA-3Cu (top: a and b) and HEA-20Cu (bottom: c and d), determined using the W – H method (left: a and c) and Scherrer formula (right: b and d), as a function of ion fluence. The dashed lines are the linear regression. Also included in (d) is the grain size determined from TEM images after 11 MeV Au irradiation to  $5.98 \times 10^{16} \text{ cm}^{-2}$ . The coefficient of determination ( $r^2$ ) is marked at the top left of the individual plots.

integrated  $E_{\text{damage}}$  decreasing by a factor of 2 (from 0.041 dpa to 0.02 dpa, and 193 to 100 keV). On the other hand, the integrated  $E_{\text{total}}$  increases significantly from 2546 to 5800 (2.3 times) and then to 11476 keV, as the Ni energy increases from 3 to 11 MeV and then to 23 MeV (Table 1). Such significant changes, the reduction in  $E_{\text{damage}}$  and increase in  $E_{\text{ionization}}$ , also shown in Fig. 1, are the underlying reason for the clear clustering (i.e., higher  $r^2$  values) observed in Fig. 2b and c, 2e and f, suggesting that inelastic thermal spikes from  $E_{\text{ionization}}$  contribute to the grain growth. This also explains the lower  $r^2$  values of 0.77 and 0.54 in Fig. 6a and b in comparison with the values of 0.80 and 0.64 shown in Fig. 2c and f: the significant contribution from  $E_{\text{ionization}}$  over the wide energy span from 3 MeV to 23 MeV is not sufficiently represented by considering only Ni ion fluence in HEA-3Cu (Fig. 6). Material modification by energetic ions under a nonequilibrium condition is different from more conventional heat treatment under thermal equilibrium [51]. Both elastic and inelastic thermal spikes lead to a distribution of vacancies, interstitial atoms, mixing atoms at GBs, and enhanced atomic motion. Although many interstitials and vacancies may be annealed primarily by close-pair recombination, high transient disorder in the microstructure along the ion path, where GB density is high, may provide a nonequilibrium environment for defects or disorder interacting with GBs to activate the instability-driven or disorder-driven mechanism [55], as observed in irradiated HEA-3Cu (Fig. 2).

The damage cascade simulations show much different behavior in HEA-20Cu than in HEA-3Cu. The atomic displacement plots show fewer displacements and a less radial distribution of displacements resulting from 3 MeV Ni ions than produced by 11 MeV Au ions (Fig. 5d and e), consistent with the results shown in Fig. 1d and e. For 23 MeV Au ions, the number and radial distribution of displacements decreases somewhat over this depth range compared with 11 MeV Au ions, consistent with the results in Fig. 1 right. As shown in Table 1, an 11 MeV Au ion deposits  $\sim 3.6$  times as much of the integrated  $E_{\text{total}}$  in the film as a 3 MeV Ni ion, even though their  $E_{\text{ionization}}/E_{\text{damage}}$  ratios are similar. On the other hand, both 11 and 23 MeV Au ions basically deposit the same

amount to  $E_{\text{total}}$ , but  $E_{\text{damage}}$  differs by a factor of  $\sim 2$  and the  $E_{\text{ionization}}/E_{\text{damage}}$  ratio changes from 2.3 to 6.1. Given the large values of  $E_{\text{ionization}}$  (6243 and 7713 keV for 11 and 23 MeV Au, respectively), the difference of 1470 keV is not as noteworthy compared with the substantial increase in  $E_{\text{ionization}}$  from 1852 to 5607 and then to 11376 keV in HEA-3Cu under Ni irradiation with increasing ion energies. Consequently, the  $E_{\text{ionization}}$  contribution via inelastic thermal spikes between 11 and 23 MeV Au ions is not apparent in Fig. 3. When  $E_{\text{damage}}$  and  $E_{\text{ionization}}$  are sizable, and the contributions are entangled as the case in HEA-20Cu, the microstructural evolution may be revealed by plotting the crystallite size as a function of ion fluence (Fig. 6). The results in Fig. 6c and d show better clustering of the data points with higher  $r^2$  values of 0.89 and 0.77, respectively, as compared with the plots in Fig. 3b and d of 0.85 and 0.70. Moreover, the Ni data (red circles) are also close to the regression lines (Fig. 6c and d). Note also that, for the most part, higher recoil energies (Fig. 4) produce defects farther from the ion trajectory and have less interaction with the electronic energy deposited by the ions. The small change in  $r^2$  values in Fig. 3 can be attributed mainly to the moderate variation in  $E_{\text{ionization}}$  under Au irradiation and to the similar  $E_{\text{ionization}}/E_{\text{damage}}$  ratio, even though the Au energies (11 and 23 MeV) are higher than the Ni energy (3 MeV).

Results in this work show that radiation effects from energetic ions should be interpreted not only in terms of atomic collision cascade processes, but also in terms of the ionizing effect induced by the localized electronic energy deposition and the resulting inelastic thermal spike, as well as the coupling between the inelastic thermal spike and collision cascade processes, even in metallic alloys. For MeV ions, both nuclear and electronic energy deposition produce transient thermal spikes and damage, as well as induce instability, and the contribution of electron energy loss cannot be ignored.

### 3.4. Comparison of thermally versus irradiation induced grain growth using *in-situ* TEM techniques

In order to evaluate differences between thermally and irradiation induced grain growth, a series of *in-situ* TEM experiments was performed. In these experiments, the microstructure of the 70 nm HEA-20Cu thin films was monitored in real-time as function of both temperature and irradiation. A particular feature of the HEA-20Cu film as-deposited is the presence of inherent nanoporosity between the nano grain boundaries, which can be assessed using underfocus bright-field TEM (BFTEM). This nanoporosity arises as a result of the magnetron-sputtered deposition at low temperatures [91]. The results from the *in-situ* TEM experiments are shown in the set of underfocus (2000 nm) BFTEM micrographs in Fig. 7 taken at RT, 553 and 773 K. For the experiments performed at elevated temperatures, the HEA-20Cu films were thermally annealed to 10 and 30 min at 573 and 773 K, respectively, and followed with Xe irradiation at the corresponding temperature. By monitoring the closure of the intragranular nanoporosity, we were able to distinguish how grain growth proceeds under annealing versus irradiation.

It can be clearly seen in Fig. 7 that irradiation at RT induces grain growth in the first 60 s of ion beam exposure. In fact, the shrinkage of nanoporosity (bright contrast areas) or disappearance of spacing between nanograins is observed in 5 s. At 573 K, the nanoporosity remains open up to 10 min of thermal annealing only; however, it closes at the first 60 s of sequential irradiation. Upon increasing the annealing and irradiation temperature to 773 K, it can be also noted that under annealing the nanoporosity does not completely vanish up to 30 min, whereas under irradiation at 773 K the nanoporosity is absent under the first 60 s. We note that, under Xe beam condition, irradiation to 2 and 60 s (i.e., ion fluence of  $1.1 \times 10^{13}$  and  $3.3 \times 10^{14} \text{ cm}^{-2}$ ) result in 0.016 and 0.48 dpa, respectively.

Grain growth induced under room temperature irradiation was compared with thermal annealing at 573 K in a previous work [45], and the results are shown in Fig. S4. The slope of the RT irradiation data displays a much steeper increase within the first 100 s but quickly decrease with increasing time to 200 s and after, suggesting a more rapid grain growth in the initial irradiation stage. Such rapid change is attributed to the disappearance of high-energy GBs in the as-deposited films, discussed in the next section. On the other hand, the relative moderate curvature observed from the 573 K annealing data suggests a slower growth process.

The results presented in Figs. 7 and S4 corroborate the idea that ion beam irradiation induces a faster kinetics of grain growth when compared with solely annealing. Such a closure of nanoporosity happens in a matter of seconds for irradiation as compared with in minutes in the pure thermal annealing cases. This directly indicates that the grain growth phenomena under irradiation is always predominant over thermal annealing for this particular HEA system. It is worth emphasizing that the *in-situ* TEM ion irradiation was carried out with lower energies than the bulk irradiation counterparts, but electron beam together with Xe ions, which although a heavier ion mass may deposit more damage energy, still presents a significant level of ionization in the samples (i.e., within the nuclear-electronic coupling regime).

### 3.5. Power law dependence HEA-20Cu

Data for 3 MeV Ni-ion-irradiated HEA-20Cu samples were chosen for further analysis because of the relatively small uncertainties of the data set. Growth of crystallites in HEA-20Cu films under 3 MeV irradiation, determined by the W – H method (diamonds) and Scherrer equation (triangles) is shown in Fig. 8. Fast growth is observed at lower fluences (see inset).

Grain growth in nanocrystalline metallic foils under ion irradiation has been reported and is explained by direct impacts of elastic thermal spikes induced by PKAs on GBs [52,58]. In this model, GB migration

occurs by atomic rearrangement within the elastic thermal spikes to reduce the local GB curvature. A power law expression of  $D^n - D_0^n = K\phi$  is derived using the number of atomic jumps across a GB resulting from the elastic thermal spike and driving force, wherein the power  $n$  value is determined to be 3 and  $K$  is related to the activation energy for atomic jumps [52].

Elastic thermal spikes from  $E_{\text{damage}}$  induced by PKAs on GBs is different from the ionization-induced inelastic thermal spike due to  $E_{\text{ionization}}$  that induces instability in local structures [51,55,92]. As shown in Sect. 3.1, both  $E_{\text{damage}}$  and  $E_{\text{ionization}}$  contribute to GB instability; thus, the power law expression is applied here to crystallite growth as a function of the total energy deposition, where  $D_0$  is the initial diameter of the columnar grains,  $\phi$  is ion fluence. The parameter  $n$  may be an intrinsic parameter depending on the material system and the dominant grain growth mechanisms [55], and  $K$  is proportional to the GB mobility of the materials and the driving force [52].

The HEA-20Cu data from the 3 MeV Ni irradiation is fitted by the expression, as shown in Fig. 8. Fitting to the average size of crystallites as a function of the total energy deposited in the HEA-20Cu film, a good agreement with the data points determined from the Scherrer equation is reached by  $D^{10} - D_0^{10} = 8 \times 10^{14} \cdot \phi$ . To keep  $n$  or  $K$  constant, either  $D^{10} - D_0^{10} = 2 \times 10^{14} \cdot \phi$ , or  $D^{10.5} - D_0^{10.5} = 8 \times 10^{14} \cdot \phi$  may be acceptable for the data determined via the W – H method. The slope of the curve drops quickly as the crystallite size increases per unit of energy deposited. Due to the existence of high-energy (i.e., GBs with high instability) and high-density GBs in the as-deposited films, the steep slope under the initial irradiation is expected. The ion fluence of  $1 \times 10^{14} \text{ cm}^{-2}$  implies that on average one ion per  $\text{nm}^{-2}$  strikes through the film. The rapid growth at the low fluence,  $\sim 1 \times 10^{14} \text{ cm}^{-2}$ , is largely attributed to the presence of very high-energy GBs in the as-deposited films, which stabilize rapidly under irradiation. Moreover, the possibilities for cascades and the inelastic spikes occurring at or near the GBs is relatively high when grain size is smaller. Upon increasing ion fluences, over  $8 \times 10^{14} \text{ cm}^{-2}$  (Fig. 8), both the number of high-energy GBs and the density of GBs drop, thus the driving forces for grain growth substantially reduce and the slope becomes gentle.

Earlier work in 1965 deliberated grain growth under a thermal driving force, and possible mechanisms were discussed in terms of the number of defects and their mobility in single-phase materials with or without second-phase particles [93]. That work showed that  $n = 2$  under a thermally driven force. Some recent studies showed higher  $n$  values, up to 3, and attributed the increase to the slower kinetics caused by solute and pore drag. Under ion irradiation via defect-driven force, the  $n$  value is suggested to be  $\sim 3$  in both metallic system [17,19,52] or nanocrystalline ceria [58,79]. In this work, the  $n$  values are determined to be 10 or 10.5, much higher than 3. In HEAs, sluggish defect migration and atomic transport are key intrinsic properties [28,29], and their impacts on damage accumulation [33] and elemental segregation [94], formation of helium bubble superlattices [95], and void swelling [74] have been reported. Sluggish diffusion is understood as shortened migration length or decreased mobility of point defects or defect clusters [1]. The origin of the sluggish diffusion effect results from atomic-level heterogeneity, especially the fluctuations in the different lattice potential energies arising from atoms migrating from site to site [42,96]. As discussed previously [26,33,42], the broken energy landscapes (i.e., the absence of continuous low-energy diffusion trajectories) modify defect migration paths from long-range 1D motion to short-range 3D motion and trap defects locally for longer times [28,74], leading to sluggish diffusion [29]. The higher  $n$  value is likely attributed to the sluggish diffusion phenomenon in nanocrystalline HEAs. The sluggish diffusion intrinsic to CSAs or HEAs is considered to be more effective than the slower kinetics caused by solute and pore drag discussed in conventional alloys. It is, therefore, expected that the more sluggish diffusion of irradiation-induced defects, the slower grain growth, and the higher  $n$  values.

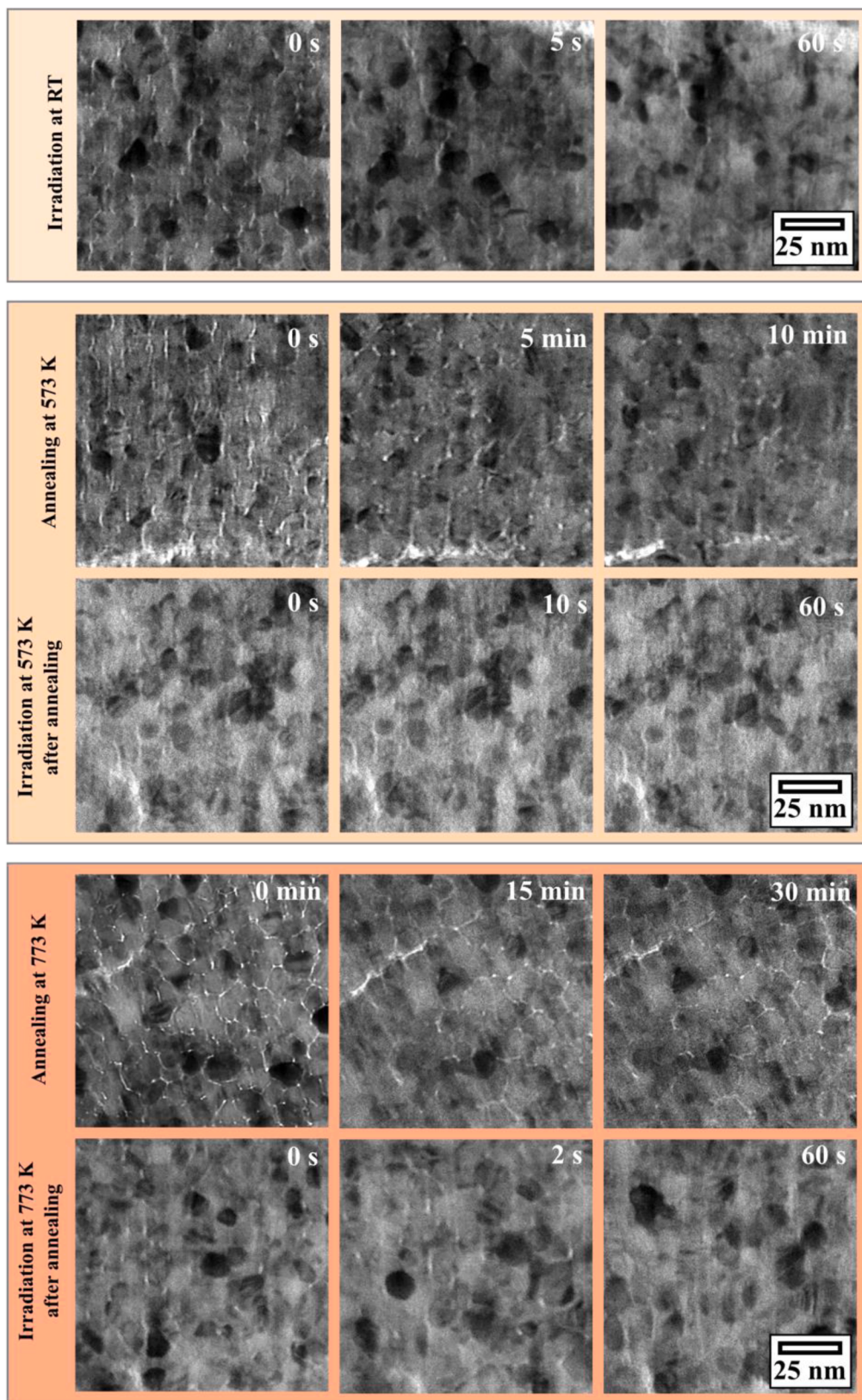


**Fig. 7.** Microstructural response of 70 nm HEA-20Cu film. Top panel: Xe irradiation at room temperature to 60 s. Middle panel: thermal annealing at 573 K up to 10 min and followed with Xe irradiation to 60 s. Bottom panel: thermal annealing at 773 K and sequential Xe irradiation up to 60 s after the thermal 30-minute annealing. By monitoring the closure of the nanoporosity using underfocus BFTEM, it can be clearly seen that the kinetics of grain growth under irradiation is significantly faster than solely driven by thermal annealing. Note: all micrographs were taken in underfocus condition (2000 nm), and scale markers at low right corners apply to all micrographs.

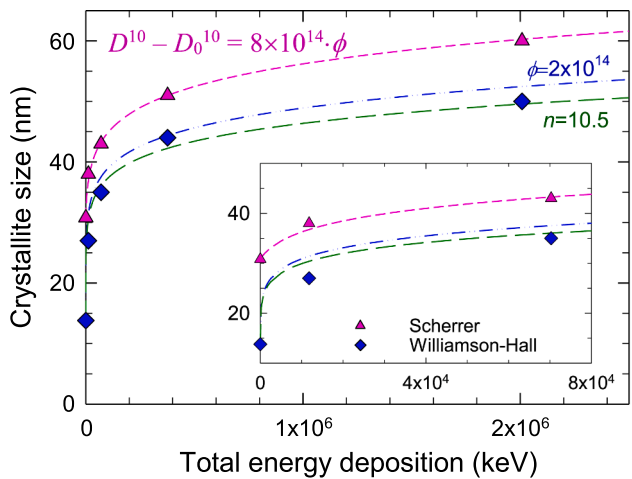


**Fig. 8.** Growth of crystallites in HEA-20Cu films under 3 MeV Ni irradiation, determined from the W – H method (diamonds) and fit to the Scherrer equation (triangles). The lines are the power law expression fit to guide the eye. In the expression  $D^n - D_0^n = K\phi$ ,  $D_0$  is the initial crystallite size, and  $\phi$  is ion fluence. The inset shows the data points and fits up to  $8 \times 10^4$  keV. The fitting parameters for the Scherrer equation are marked on the plot. The parameters  $n$  and  $K$  for the W – H method are 10 and  $2 \times 10^{14}$  (dashed-dotted line) or 10.5 and  $8 \times 10^{14}$  (long-dashed line), respectively.

### 3.6. Electronic and atomic response of ceramics structures and metallic alloys to irradiation

Electronic and atomic response of ceramics structures and metallic alloys to irradiation, either in single crystals or polycrystals, can be viewed from the competition between the inelastic thermal spikes via electron–phonon coupling and elastic thermal spikes via collisions among atomic nuclei, or viewed from their bond characteristics. Coupled electronic and atomic energy dissipation can lead to *synergistic*, *additive*, and *competitive* effects in terms of defect production. The *synergistic* interactions occur, due to the presence of collisional defects, that can sensitize a material to electronic energy loss effects and result in substantially more damage production (amorphous tracks) than would occur from the sum of damage production processes from electronic and ballistic processes. *Additive* effects can occur, where the electronic and ballistic energy loss processes from a single ion combine to produce more damage (amorphization) or microstructural change (grain growth) than can be expected from ballistic collisional processes alone. The *competitive* interactions are associated with in-cascade defect annealing and recovery resulting in overall damage reduction. While highly ionizing ions, such as GeV ions, may not produce amorphous or damage tracks in pristine structures, electronic energy deposition from MeV ions interacts synergistically with the preexisting defects in which significant damage production or annealing can occur. As examples, experiments and molecular dynamics simulations have shown the distinctive evidence of ionizing effects that affect the dynamic response of materials in single crystal or nanocrystalline form to irradiation, including *synergistic* effects in SrTiO<sub>3</sub> [60], *additive* effects in nanocrystalline CeO<sub>2</sub> and ZrO<sub>2</sub> [55,92] and in ZrSiO<sub>4</sub> [97], and *competitive* effects in SiC [98,99]. Clear impact of electronic and atomic energy exchanges on defect production and evolution is also demonstrated in CSAs [32,62,88]. In CSAs, more pronounced electronic effects are observed in chemically more complex alloys that MeV ions may induce elastic strain relaxation of existing defects and defect clusters [32] but the extreme electronic energy deposition from GeV ions can lead to damage formation [88], both attributing to lower thermal conductivity and stronger *e-ph* coupling. Transition metals with unique electronic structures may be selected to tune the *e-ph* coupling strength and heat capacity, which affect locally energy dissipation and defect annealing.

Structural or phase stability under ion irradiation can be viewed from the competition between the elastic and inelastic thermal spikes. The strong temporal and spatial coupling of electronic and ballistic energy dissipation processes to the lattice plays an important role in competitive in-cascade recovery and additive in-cascade damage production, as well as additive thermal spikes. More specifically, intense electronic energy deposition may result in a rapid, nonlinear increase in damage production (the synergistic effect) and even lead to full amorphization (e.g., in some ABO<sub>3</sub> oxides) [60,100]. There is a significant reduction in the incubation fluence for rapid amorphization with the increasing amount of accumulated damage, and the amorphous cross sections exhibit a linear dependence on the initial disorder level. On the other hand, ionization may induce significant defect annihilation and amazingly restore lattice order (the competitive effect). Both synergistic (damaging) or competitive (annealing) effects can occur in the same material with electronic stopping power either above or below a threshold, demonstrating complex interactions between inelastic energy deposition and preexisting atomic defects. The dominate electronic effect, *synergistic*, *additive*, or *competitive*, in chemically complex materials may be associated with the local melting temperature along the ion track, which in turn depends on both the host material properties and local damage states. There is a competition from the localized thermal and athermal effects: melting with a rapid quench may lead to more defects (synergistic effect) but considerable athermal processes that lower the energy barriers may result in more annealing (competitive effect). For example, in a more damaged region when energy/heat dissipates slower and local *e-ph* coupling is stronger, it is more likely to meet local melting condition and thus results in more defects (i.e., synergistic effect). On the contrary, ionizing-induced inelastic thermal spikes may anneal the pre-existing defects.

Ionizing ions modifying materials properties by reordering or amorphizing the local atomic arrangement may also be viewed from the atomic bonding. In recent years, the importance of ionization effects and the coupled processes has become increasingly recognized for materials with ionic, covalent, and metallic bonds [25,51,101]. Radiation effect studies in ceramic materials have shown dissimilar response to damage or amorphization resulting from the competition between the short-range covalent and long-range ionic forces. For many alloys composed of multiple transition metals, although metallic bonding is considered as many positively charged nuclei surrounded by an electron cloud of valence electrons that are not localized, the existence of directional bonding, valence charge redistribution, and covalent characteristic have been discussed in some recent studies [102,103]. Although more quantified studies were conducted for nanocrystalline SiC (very strong tetrahedral covalent bonding) [104], ZrC (strong covalent Zr-C bond but less covalent than Si-C bond) [79], CeO<sub>2</sub> and ZrO<sub>2</sub> (mixed ionic-covalent bonding) [51,55,57,58,92] under irradiation at room or low temperature, knowledge on the role of bond characteristics and electronic deformability on materials properties in ionically/covalently bonded ceramics with multiple cation substitutions is rather scarce, and this likewise holds true for complex concentrated alloys or HEAs.

Understanding mechanisms of grain growth in CSAs is still in the initial basic science stage. Elemental-specific tunable alloy properties in CSAs imply elemental-specific or biased defect processes and interface stability under nonequilibrium conditions. The separable and distinct effects of ionization-induced recovery processes may be conducted to understand and model the complex damage accumulation behavior observed in CSAs and other ceramics by varying nuclear energy loss ( $S_n$ ), electronic energy loss ( $S_e$ ), and the electronic-to-nuclear energy loss ratio ( $S_e/S_n$ ) along channeling or off-channel directions. This approach provides a path forward to investigate, delineate, and understand athermal effects. Such effort may provide better understanding of cation disorder in single-phase complex ceramics, as well as chemical heterogeneity from the elemental diversity in high-entropy materials (e.g., high-entropy ceramics and CSAs).

Combining the chemical complexity and microstructural complexity

(e.g., interfaces and grain boundaries) in concentrated alloys may be an innovative approach to maximize the ability of controlling mass transport and defect dynamics, thereby enhancing materials properties (e.g., defect tolerance and structural stability). It is, however, challenging to obtain a more quantitative assessment of the role of electronic energy loss before an in-depth understanding of defect dynamics in CSAs is available. The power law expression or the thermal spike model of grain growth, used in this work, can be applied to interpret the observed irradiation grain growth in the context of irradiation parameters [58], even though the model was originally established to describe metallic systems under thermal annealing. This recent work [58] emphasize a better understanding of radiation conditions and material properties, as there are complex relationships between irradiation dose, dose rate, and temperature on defect density, and their effects on grain boundary mobility. More quantitative interpretation of sluggish diffusion on grain growth requires more integrated experiments, theory and modeling efforts.

#### 4. Conclusion

In the past several years, significant modeling effort and experimental characterization of irradiated CSAs have revealed that improved radiation performance is attributed to inefficient formation of defect clusters from cascades events, locally slow heat dissipation, and consequentially improved defect annihilation, which together ultimately suppress damage accumulation and the growth of extended defects. In this work, we study the stability of nanocrystalline HEAs under ion irradiation and demonstrate the role of electronic energy deposition and dissipation in chemically complex alloys.

The fcc phase in nanocrystalline  $(\text{NiFeCoCr})_{97}\text{Cu}_3$  and  $\text{Ni}_{20}\text{Fe}_{20}\text{Co}_{20}\text{Cr}_{20}\text{Cu}_{20}$  is stable under Ni and Au irradiation up to 23 MeV to high fluences. Energetic charged particles, such as MeV heavy ions, deposit a significant amount of energy both into the electronic subsystem, leading to inelastic thermal spikes along the ion paths, and into the atomic subsystem, causing elastic thermal spikes that are absorbed by the creation of atomic displacements. Heavy ions of Ni and Au at different energies are chosen to deposit ionizing energy and damage energy in the HEA films at different rates and ratios. Grain growth is observed, but the growth rate is much slower than in conventional dilute alloys. Although the large numbers of defects resulting from displacement events contribute to grain growth, the strong correlation of the data points on the total energy deposition over a wide range of Ni energies suggests that atomic displacement processes are not the only contribution—electron energy loss also plays an important role. Moreover, differences in primary defect structure and spatial distribution between Ni and Au irradiation should be considered.

Crystallite growth follows a power law dependence with deposited energy. The high power  $n$  value suggests a significant contribution from the irradiation-induced instability at and near GBs that leads to locally rapid atomic rearrangements and grain growth. Irradiation-induced structural instability and crystallite growth is more significant in small grains but less effective in larger grains, as sluggish diffusion results in fewer defects migrating to and annealing at the GBs or interfaces. Compared with nanocrystalline metals and radiation-resistant nanocrystalline oxide films that have periodic lattice structure, and thus periodic electronic structure and energy landscapes, the much slower radiation-induced microstructural evolution (e.g., slower growth rate) in nanocrystalline HEAs may be attributed to the sluggish diffusion and the resulting slower kinetics. Growth of grains or crystallites in nanocrystalline materials is often thermally activated, but it can also be driven by irradiation at much lower temperatures owing to the presence of defects and radiation-induced microstructural instabilities. The unraveling of mechanisms on coupling the inelastic and elastic thermal spikes opens new possibilities for better control of grain sizes of nanocrystalline HEAs at relatively low temperatures.

In a broader perspective, understanding the coupling of electronic

and atomic processes in the intermediate MeV energy regime, where both  $E_{\text{damage}}$  and  $E_{\text{ionization}}$  are large and comparable, is critically important; it is the energy regime used for ion simulation of radiation effects in nuclear environments; for ion implantation doping, ion-beam materials modification and defect engineering by research institutions and industry; and for ion-beam analytical techniques. Understanding the energy transport in materials over multiple time and length scales and subsequent nonlinear defect dynamics and phase stability from the level of electrons and atoms will thus help to address questions that span many research areas of condensed matter physics. This study and previously findings reported in literature provide clear evidence of and important arguments for non-negligible ionization effects on the kinetics of atomic processes under ion irradiation. Ion irradiation will continue to be utilized for radiation effect studies, and this work calls attention to quantified fundamental understanding of radiation damage processes beyond much simplified displacement events, especially in simulating neutron environments.

#### Declaration of Competing Interest

The authors declare that they have no known competing financial interests or personal relationships that could have appeared to influence the work reported in this paper.

#### Acknowledgements

This work was supported as part of Energy Dissipation to Defect Evolution (EDDE), an Energy Frontier Research Center funded by the U.S. Department of Energy, Office of Science, Basic Energy Sciences, under contract number DE-AC05-00OR22725. The ion irradiations were performed at the Ion Beam Materials Laboratory located at the University of Tennessee, Knoxville. PDR acknowledges support from the Center for Nanophase Materials Sciences from the U.S. Department of Energy (DOE) under grant No# KC0403040 ERKCZ01. MAT was supported by the Laboratory Directed Research and Development program of the Los Alamos National Laboratory under project number 20200689PDR2. MAT and SED acknowledge support from the Engineering and Physical Sciences Research Council (EPSRC) for funding the MIAMI facility under the grants EP/E017266/1 and EP/M028283/1. MAT would like to thank Dr. Graeme Greaves (University of Huddersfield) for assistance with the in-situ TEM experiments herein presented.

#### Appendix A. Supplementary data

Supplementary data to this article can be found online at <https://doi.org/10.1016/j.coSSMS.2022.101001>.

#### References

- [1] Y. Zhang, Y.N. Osetsky, W.J. Weber, Tunable Chemical Disorder in Concentrated Alloys: Defect Physics and Radiation Performance, *Chem. Rev.* 122 (2022) 789–829, <https://doi.org/10.1021/acs.chemrev.1c00387>.
- [2] E.J. Pickering, A.W. Carruther, P.J. Barron, S.C. Middleburgh, D.E.J. Armstrong, A.S. Gandy, High-Entropy Alloys for Advanced Nuclear Applications, *Entropy* 23 (2021) 98, <https://doi.org/10.3390/e23010098>.
- [3] G.S. Was, Fundamentals of Radiation in Materials—Chapter 11: Simulation of Neutron Irradiation Effects with Ions, Springer, Berlin, Heidelberg, New York, 2007.
- [4] G.S. Was, Z. Jiao, E. Getto, K. Sun, A.M. Monterrosa, S.A. Maloy, O. Anderoglu, B. H. Sencer, M. Hackett, Emulation of reactor irradiation damage using ion beams, *Scri. Mater.* 88 (2014) 33–36.
- [5] Accelerator Simulation and Theoretical Modelling of Radiation Effects in Structural Materials, IAEA Nuclear Energy Series Publications, No. NF-T-2.2, Structure of The IAEA Nuclear Energy Series, September (2018). ISSN 1995–7807, IAEAL 18-01158 | ISBN 978-92-0-107415-7.
- [6] G.S. Was, Fundamentals of Radiation Materials Science: Metals and Alloys, Springer, 2017.
- [7] H. Wiedersich, P. Okamoto, N.Q. Lam, A theory of radiation-induced segregation in concentrated alloys, *J. Nucl. Mater.* 83 (1979) 98–108.

- [8] G.S. Was, J.P. Wharry, B. Frisbie, B.D. Wirth, D. Morgan, J.D. Tucker, T.R. Allen, Assessment of radiation-induced segregation mechanisms in austenitic and ferritic-martensitic alloys, *J. Nucl. Mater.* 411 (2011) 41–50.
- [9] A.J. Ardell, P. Bellon, Radiation-induced solute segregation in metallic alloys, *Curr. Opin. Solid State Mater. Sci.* 20 (2016) 115–139.
- [10] T. Schuler, D.R. Trinkle, P. Bellon, R. Averback, Design principles for radiation-resistant solid solutions, *Phys. Rev. B* 95 (2017), 174102.
- [11] T.R. Allen, G. Was, Modeling radiation-induced segregation in austenitic Fe–Cr–Ni alloys, *Acta Mater.* 46 (1998) 3679–3691.
- [12] R. Averback, T.D. De La Rubia, H. Hsieh, R. Benedek, Interactions of energetic particles and clusters with solids, *Nucl. Instrum. Methods Phys. Res. B* 59 (1991) 709–717.
- [13] S.J. Pejchal, L. Snead, Z.S. Hartwig, Intermediate energy proton irradiation: Rapid, high-fidelity materials testing for fusion and fission energy systems, *Mater. Des.* 200 (2021), 109445.
- [14] I. Beyerlein, A. Caro, M. Demkowicz, N. Mara, A. Misra, B. Uberuaga, Radiation damage tolerant nanomaterials, *Mater. Today* 16 (2013) 443–449.
- [15] A. Hirata, T. Fujita, Y. Wen, J. Schneibel, C.T. Liu, M. Chen, Atomic structure of nanoclusters in oxide-dispersion-strengthened steels, *Nat. Mater.* 10 (2011) 922.
- [16] G. Liu, G. Zhang, F. Jiang, X. Ding, Y. Sun, J. Sun, E. Ma, Nanostructured high-strength molybdenum alloys with unprecedented tensile ductility, *Nat. Mater.* 12 (2013) 344.
- [17] D.E. Alexander, G.S. Was, Thermal-spike treatment of ion-induced grain growth: Theory and experimental comparison, *Physical Review B* 47 (1993) 2983.
- [18] W. Voegeli, K. Albe, H. Hahn, Simulation of grain growth in nanocrystalline nickel induced by ion irradiation, *Nuclear Instruments and Methods in Physics Research B* 202 (2003) 230–235.
- [19] J.C. Liu, J. Li, J.W. Mayer, Temperature effect on ion-irradiation-induced grain growth in Cu thin films, *J. Appl. Phys.* 67 (1990) 2354–2358.
- [20] B. Cantor, I. Chang, P. Knight, A. Vincent, Microstructural development in equiatomic multicomponent alloys, *Mater. Sci. and Eng. A* 375 (2004) 213–218.
- [21] B. Cantor, Multicomponent and high entropy alloys, *Entropy* 16 (9) (2014) 4749–4768.
- [22] J.W. Yeh, Y. L. Chen, S. J. Lin, S. K. Chen, High-entropy alloys—a new era of exploitation, in: *Materials Science Forum*, Vol. 560, Trans Tech Publ, 2007, pp. 1–9.
- [23] C.-Y. Cheng, Y.-C. Yang, Y.-Z. Zhong, Y.-Y. Chen, T. Hsu, J.-W. Yeh, Physical metallurgy of concentrated solid solutions from low-entropy to high-entropy alloys, *Curr. Opin. Solid State Mater. Sci.* 21 (2017) 299–311.
- [24] Y. Zhang, K. Jin, H. Xue, C. Lu, R. Olsen, L. Beland, M.W. Ullah, S. Zhao, H. Bei, D. S. Aidhy, G.D. Samolyuk, L. Wang, M. Caro, A. Caro, G.M. Stocks, B.C. Larson, I. M. Robertson, A.A. Correa, W.J. Weber, Influence of Chemical Disorder on Energy Dissipation and Defect Evolution in Advanced Alloys, *J. Materials Research* 31 (2016) 2363–2375.
- [25] Y. Zhang, S. Zhao, W.J. Weber, K. Nordlund, F. Granberg, F. Djurabekova, Atomic-level heterogeneity and defect dynamics in concentrated solid-solution alloys, *Curr. Opin. Solid State Mater. Sci.* 21 (2017) 221–237.
- [26] Y. Zhang, T. Egami, W.J. Weber, Dissipation of radiation energy in concentrated alloys: Unique defect properties and microstructural evolution, *MRS Bull.* 44 (2019) 798–811.
- [27] Y. Osetsky, A.V. Barashev, L.K. Béland, Z. Yao, K. Ferasat, Y. Zhang, Tunable chemical complexity to control atomic diffusion in alloys, *npj Comput. Mater.* 6 (38) (2020) 492.
- [28] Y.N. Osetsky, L. Béland, A. Barashev, Y. Zhang, On the existence and origin of sluggish diffusion in chemically disordered concentrated alloys, *Curr. Opin. Solid State Mater. Sci.* 22 (2018) 65–74.
- [29] Y.N. Osetsky, A. Barashev, Y. Zhang, Sluggish, Chemical Bias and Percolation Phenomena in Atomic Transport by Vacancy and Interstitial Diffusion in Ni-Fe alloys, *Curr. Opin. Solid State Mater. Sci.* 25 (2021), 100961.
- [30] Y. Zhang, G.M. Stocks, K. Jin, C. Lu, H. Bei, B.C. Sales, L. Wang, L.K. Béland, R. E. Stoller, G.D. Samolyuk, M. Caro, A. Caro, W.J. Weber, Influence of chemical disorder on energy dissipation and defect evolution in nickel and Ni-based concentrated solid-solution alloys, *Nat. Commun.* 6 (2015) 8736.
- [31] G. Velisa, E. Wendler, S. Zhao, K. Jin, H. Bei, W.J. Weber, Y. Zhang, Delayed damage accumulation by athermal suppression of defect production in concentrated solid solution alloys, *Mater. Res. Lett.* 6 (2018) 136–141.
- [32] N. Sellami, A. Debelle, M.W. Ullah, H.M. Christen, J.K. Keum, H. Bei, H. Xue, W. J. Weber, Y. Zhang, Effect of electronic energy dissipation on strain relaxation in irradiated concentrated solid solution alloys, *Curr. Opin. Solid State Mater. Sci.* 23 (2019) 107–115.
- [33] Y. Zhang, X. Wang, Y. Osetsky, Y. Tong, R. Harrison, S.E. Donnelly, Y. Di Chen, H. Wang, B.C. Bei, K.L. Sales, P. More, L. Xiu, W.J.W. Wang, Effects of 3d electron configurations on helium bubble formation and void swelling in concentrated solid-solution alloys, *Acta Mater.* 181 (2019) 519–529.
- [34] C.C. Koch, Nanocrystalline high-entropy alloys, *J. Mater. Res.* 32 (2017) 3435.
- [35] Y. Zou, J.M. Wheeler, H. Ma, P. Okle, R. Spolenak, Nanocrystalline High-Entropy Alloys: A New Paradigm in High Temperature Strength and Stability, *Nano Lett.* 17 (2017) 1569–1574.
- [36] Z. Fu, W. Chen, H. Wen, D. Zhang, Z. Chen, B. Zheng, Y. Zhou, E.J. Lavernia, Microstructure and strengthening mechanisms in an FCC structured single-phase nanocrystalline Co<sub>25</sub>Ni<sub>25</sub>Fe<sub>25</sub>Al<sub>7.5</sub>Cu<sub>17.5</sub> high-entropy alloy, *Acta Mater.* 107 (2016) 59–71.
- [37] Weibing Liao, Si Lan, Libo Gao, Hongti Zhang, Shang Xu, Jian Song, Xunli Wang, Yang Lu, Nanocrystalline high-entropy alloy (CoCrFeNiAl0.3) thin-film coating by magnetron sputtering, *Thin Solid Films* 638 (2017) 383–388.
- [38] Gowtham Sriram Jawaharam, Christopher M. Barr, Anthony M. Monterrosa, Khalid Hattar, Robert S. Averback, Shen J. Dillon, Irradiation induced creep in nanocrystalline high entropy alloys, *Acta Materialia* 182 (2020) 68–76.
- [39] E. Levo, F. Granberg, D. Utt, K. Albe, K. Nordlund, F. Djurabekova, Radiation stability of nanocrystalline single-phase multicomponent alloys, *J. Mater. Res.* 34 (5) (2019) 854–866, <https://doi.org/10.1557/jmr.2019.19>.
- [40] M.A. Tunes, G. Greaves, P.D. Rack, W.L. Boldman, C.G. Schön, S. Pogatscher, S. A. Maloy, Y. Zhang, O. El Atwani, Irradiation stability and induced ferromagnetism in a nanocrystalline CoCrCuFeNi highly-concentrated alloy, *Nanoscale* 13 (2021) 20437–20450.
- [41] E. Lu, J. Zhao, I. Makkonen, K. Mizohata, Z. Li, M. Hua, F. Djurabekova, F. Tuomisto, Enhancement of vacancy diffusion by C and N interstitials in the equiatomic FeMnNiCoCr high entropy alloy, *Acta Mater.* 215 (2021), 117093.
- [42] S. Zhao, Y. Zhang, W.J. Weber, Engineering defect energy landscape of CoCrFeNi high-entropy alloys by the introduction of additional dopants, *J. Nucl. Mater.* 561 (2022), 153573.
- [43] O. El-Atwani, N. Li, M. Li, A. Devaraj, J.K.S. Baldwin, M.M. Schneider, D. Sobieraj, J.S. Wróbel, D. Nguyen-Manh, S.A. Maloy, E. Martinez, Outstanding radiation resistance of tungsten-based high-entropy alloys, *Sci. Adv.* 5 (2019) eaav2002.
- [44] Q. Lin, X. An, H. Liu, Q. Tang, P. Dai, X. Liao, In-situ high-resolution transmission electron microscopy investigation of grain boundary dislocation activities in a nanocrystalline CrMnFeCoNi high-entropy alloy, *J. Alloy. Compd.* 709 (2017) 802–807.
- [45] Y. Zhang, M.A. Tunes, M.L. Crespiello, F. Zhang, W.L. Boldman, P.D. Rack, L. Jiang, C. Xu, G. Greaves, S.E. Donnelly, L. Wang, W.J. Weber, Thermal Stability and Irradiation Response of Nanocrystalline CoCrCuFeNi High-entropy Alloy, *Nanotechnology: Focused Issue on Ion Beam Technology* 30 (2019), 294004.
- [46] M.A. Tunes, V.M. Vishnyakov, O. Camara, G. Greaves, P.D. Edmondson, Y. Zhang, S.E. Donnelly, A candidate accident tolerant fuel system based on a highly concentrated alloy thin film, *Mater. Today, Energy* 12 (2019) 356–362.
- [47] L. Jiang, Y. Hu, K. Sun, P. Xiu, M. Song, Y. Zhang, W.L. Boldman, M.L. Crespiello, P.D. Rack, L. Qi, W.J. Weber, L. Wang, Irradiation-Induced Extremes Create Hierarchical Face-to-Body-Centered Cubic Phases in Nanostructured High Entropy Alloys, *Adv. Mater.* (2020) 2002652, <https://doi.org/10.1002/adma.202002652>.
- [48] Y. Guo, M. Li, P. Li, C. Chen, Q. Zhan, Y. Chang, Y. Zhang, Microstructure and mechanical properties of oxide dispersion strengthened FeCoNi concentrated solid solution alloys, *J. of Alloys and Compounds* 820 (2020), 153104.
- [49] M. Li, C. Chen, P. Li, W. Li, Y. Guo, Q. Ji, Y. Zhang, Y. Chang, Oxide dispersion strengthened FeCoNi concentrated solid-solution alloys synthesized by mechanical alloying, *Intermetallics* 117 (2020), 106674.
- [50] W. Li, X. Zhan, X. Song, S. Si, R. Chen, J. Liu, Z. Wang, J. He, X. Xiao, A Review of Recent Applications of Ion Beam Techniques on Nanomaterial Surface Modification: Design of Nanostructures and Energy Harvesting, *Small* 15 (2019) 1901820.
- [51] Y. Zhang, W.J. Weber, Ion irradiation and modification: coupled electronic and nuclear energy dissipation and subsequent non-equilibrium processes in materials, *Appl. Phys. Rev.* 7 (2020), 041307.
- [52] D. Kaoumi, A.T. Motta, R.C. Biritchi, A thermal spike model of grain growth under irradiation, *J. Appl. Phys.* 104 (2008), 073525.
- [53] J.C. Liu, M. Nastasi, J. w., Mayer Ion irradiation induced grain growth in Pd polycrystalline thin films, *J. Appl. Phys.* 62 (1987) 423.
- [54] H.A. Atwater, C.V. Thompson, H.I. Smith, Ion-bombardment-enhanced grain growth in germanium, silicon, and gold thin films, *J. Appl. Phys.* 64 (1988) 2337.
- [55] Y. Zhang, D.S. Aidhy, T. Varga, S. Moll, P.D. Edmondson, F. Namavar, K. Jin, C. N. Ostroumov, W.J. Weber, The effect of electronic energy loss on irradiation induced grain growth in nanocrystalline oxides, *PCCP* 16 (2014) 8051–8059.
- [56] P.D. Edmondson, Y. Zhang, S. Moll, F. Namavar, W.J. Weber, Irradiation effects on microstructure change in nanocrystalline ceria – Phase, lattice stress, grain size and boundaries, *Acta Mater.* 60 (2012) 5408–5416.
- [57] W.-Y. Chen, M. Li, R. Sisson, P. Baldo, Z. Yu, C. Ulmer, A.T. Motta, IVM Contributions to CINR Penn State MT17-12797: In situ Ion Irradiation to Add Irradiation Assisted Grain Growth to the MARMOT Tool. United States: N. p., 2021, Web. doi:10.2172/1822201.
- [58] C.J. Ulmer, W.-Y. Chen, D.E. Wolfe, A.T. Motta, In-situ ion irradiation induced grain growth in nanocrystalline ceria, *J. Nucl. Mater.* 545 (2021), 152688.
- [59] N.J. Madden, S.A. Briggs, D. Perales, T.J. Boyle, K. Hattar, J.A. Krogstad, Measuring Radiation Enhanced Diffusion Through in situ Ion Radiation Induced Sintering of Oxide Nanoparticles. Available at SSRN: <https://ssrn.com/abstract=3951050> or <https://doi.org/10.2139/ssrn.3951050>.
- [60] W.J. Weber, D.M. Duffy, L. Thomé, Y. Zhang, The role of electronic energy loss in ion beam modification of materials, *Curr. Opin. Solid State Mater. Sci.* 19 (2015) 1–11.
- [61] K. Jin, B.C. Sales, G.M. Stocks, G.D. Samolyuk, M. Daene, W.J. Weber, Y. Zhang, H. Bei, Tailoring the physical properties of Ni-containing single-phase equiatomic alloys by modifying the chemical complexity, *Sci. Rep.* 6 (2016) 20159.
- [62] R. Sachan, M.W. Ullah, M.F. Chisholm, J. Liu, P. Zhai, D. Schaures, P. Kluth, C. Trautmann, H. Bei, W.J. Weber, Y. Zhang, Radiation-induced extreme elastic and inelastic interactions in concentrated solid solutions, *Mater. Des.* 150 (2018) 1–8.
- [63] M.W. Ullah, N. Sellami, A. Leino, H. Bei, Y. Zhang, W.J. Weber, Electron-phonon coupling induced defect recovery and strain relaxation in Ni and equiatomic NiFe alloy, *Comput. Mater. Sci.* 173 (2020), 109394.

- [64] Z. Wu, M.C. Troparevsky, Y.F. Gao, J.R. Morris, G.M. Stocks, H. Bei, Phase stability, physical properties and strengthening mechanisms of concentrated solid solution alloys, *Curr. Opin. Solid State Mater. Sci.* 21 (2017) 267–284.
- [65] S. San, Y. Tong, H. Bei, B. Kombaiah, Y. Zhang, W.-Y. Ching, First-principles calculation of lattice distortions in four single phase high entropy alloys with experimental validation, *Mater. Des.* 209 (2021) 1100712.
- [66] T. Nagasse, P.D. Rack, J.H. Noh, T. Egami, In-situ TEM observation of structural changes in nano-crystalline CoCrCuFeNi multicomponent high-entropy alloy (HEA) induced under fast electron irradiation by high voltage electron microscopy (HVEM), *Intermetallics* 59 (2015) 32.
- [67] Z. An, H. Jia, Y. Wu, P.D. Rack, A.D. Patchen, Y. Liu, Y. Ren, N. Li, P.K. Liaw, Solid-Solution CrCoCuFeNi High-Entropy Alloy Thin Films Synthesized by Sputter Deposition, *Mater. Res. Lett.* 3 (2015) 203–209.
- [68] R.W. Harrison, J.A. Hinks, S.E. Donnelly, Influence of pre-implanted helium on dislocation loop type in tungsten under self-ion irradiation, *Scr. Mater.* 150 (2018) 61.
- [69] W.J. Weber, Y. Zhang, Predicting Damage Production in Monoatomic and Multi-elemental Targets using Stopping and Range of Ions in Matter Code: Challenges and Recommendations, *Curr. Opin. Solid State Mater. Sci.* 23 (2019), 100757.
- [70] Y. Zhang, M.L. Crespillo, H. Xue, K. Jin, C.H. Chen, C.L. Fontana, J.T. Graham, W. J. Weber, New ion beam materials laboratory for materials modification and irradiation effects research, *Nucl. Instrum. Methods Phys. Res. B* 338 (2014) 19–30.
- [71] J. F. Ziegler, J. P. Biersack, M. D. Ziegler, The Stopping and Range of Ions in Solids (SRIM Co. 2008), as well as the original book of by J. F. Ziegler, J. P. Biersack, and U. Littmark, (Pergamon, New York, 1985). J. F. Ziegler, SRIM-2013 software package, available online at <http://www.srim.org>.
- [72] R.E. Stoller, M.B. Toloczko, G.S. Was, A.G. Certain, S. Dwaraknath, F.A. Garner, Erratum to “On the use of SRIM for computing radiation damage exposure”, *Nucl. Instrum. Methods Phys. Res.* 459 (2019) 196–197.
- [73] C. Ostrouchov, Y. Zhang, W.J. Weber, pySRIM : Automation, Analysis, and Plotting of SRIM Calculations, *J. Open Source Softw.* 3 (2018) 10–12.
- [74] C. Lu, L. Niu, N. Chen, K. Jin, T. Yang, P. Xiu, Y. Zhang, F. Gao, H. Bei, S. Shi, M. R. He, I.M. Robertson, W.J. Weber, L. Wang, Enhancing radiation tolerance by controlling defect mobility and migration pathways in multicomponent single phase alloys, *Nat. Commun.* 7 (2016) 13564.
- [75] A.C. Larson, R.B. Von Dreele, General Structure Analysis System (GSAS), Los Alamos National Laboratory Report LAUR (2000) 86–748.
- [76] D.S. Moore, W.I. Notz, M. A. Fligner, The basic practice of statistics (6th ed.). New York, NY: W. H. Freeman and Company. (2013) Page 138.
- [77] D.S. Aidhy, C. Lu, K. Jin, H. Bei, Y. Zhang, L. Wang, W.J. Weber, Point defect evolution in Ni, NiFe and NiCr alloys from atomistic simulations and irradiation experiments, *Acta Mater.* 99 (2015) 69–76.
- [78] L.K. Béland, Y.N. Ossetsky, R.E. Stoller, Atomistic material behavior at extreme pressures, *npj Comput. Mater.* 2 (2016) 16007.
- [79] C.J. Ulmer, A.T. Motta, Modeling thermal spike driven reactions at low temperature and application to zirconium carbide radiation damage, *Nucl. Instrum. Methods Phys. Res. B* 410 (2017) 200.
- [80] Y. Zhang, W. Jiang, C. Wang, F. Namavar, P.D. Edmondson, Z. Zhu, F. Gao, J. Lian, W.J. Weber, Grain growth and phase stability of nanocrystalline cubic zirconia under ion irradiation, *Physical Review B* 82 (2010), 184105.
- [81] E. Levo1, F. Granberg, D. Utt, K. Albe, K. Nordlund, F. Djurabekova, Radiation stability of nanocrystalline single-phase multicomponent alloys, *J. Mat. Res.* 34 (2019) 854–866.
- [82] Y. Zhang, P.D. Edmondson, T. Varga, S. Moll, F. Namavar, C. Lan, W.J. Weber, Structural Modification of Nanocrystalline Ceria by Ion Beams, *PCCP* 13 (2011) 11946–11950.
- [83] Y.-Q. Chang, Q. Guo, J. Zhang, L. Chen, Y. Long, F.-R. Wan, Irradiation effects on nanocrystalline materials, *Front. Mater. Sci.* 7 (2013) 143–155.
- [84] Y. Chang, Y. Guo, M. Li, K. Wang, L. Lv, D. Liu, Effects of crystal quality, grainsize and oxygen vacancy of nanocrystalline CeO<sub>2</sub> films under 1.5 MeV Au ion irradiation, *J. Nucl. Mater.* 518 (2019) 41–47.
- [85] A. Kilmametov, A. Balogh, M. Ghafari, C. Gammer, C. Mangler, C. Rentenberger, R. Valiev, H. Hahn, Radiation effects in bulk nanocrystalline FeAl alloy, *Radiat. Eff. Defects Solids* 167 (2012) 631–639.
- [86] Y. Zhang, H. Xue, E. Zarkadoula, R. Sachan, C. Ostrouchov, P. Liu, X. Wang, S. Zhang, T.S. Wang, W.J. Weber, Coupled electronic and atomic effects on defect evolution in silicon carbide under ion irradiation, *Curr. Opin. Solid State Mater. Sci.* 21 (2017) 285–298.
- [87] E. Zarkadoula, G. Samolyuk, W.J. Weber, Effects of electronic excitation in 150 keV Ni ion irradiation of metallic systems, *AIP Adv.* 8 (2018), 015121.
- [88] A. Leino, G.D. Samolyuk, R. Sachan, F. Granberg, W.J. Weber, H. Bei, J. Liu, P. Zhai, Y. Zhang, GeV ion irradiation of NiFe and NiCo: Insights from MD simulations and experiments, *Acta Mater.* 151 (2018) 191–200.
- [89] E. Zarkadoula, G. Samolyuk, W.J. Weber, Effects of electron–phonon coupling on damage accumulation in molecular dynamics simulations of irradiated nickel, *Mater. Res. Lett.* 7 (2019) 490–495.
- [90] R.S. Averback, Atomic displacement processes in irradiated metals, *J. Nucl. Mater.* 216 (1994) 49–62, [https://doi.org/10.1016/0022-3115\(94\)90006-X](https://doi.org/10.1016/0022-3115(94)90006-X).
- [91] J.A. Thornton, The microstructure of sputter-deposited coatings, *J. Vac. Sci. Technol. A Vacuum, Surfaces, Film.* 4 (1986) 3059–3065.
- [92] D.S. Aidhy, Y. Zhang, W.J. Weber, A fast grain-growth mechanism revealed in nanocrystalline ceramic oxides, *Scr. Mater.* 83 (2014) 9–12.
- [93] M. Hillert, On the theory of normal and abnormal grain growth, *Acta Metall.* 13 (1965) 227–238.
- [94] A. Barashev, Y.N. Ossetsky, H. Bei, C. Lu, L. Wang, Y. Zhang, Chemically-Biased Diffusion and Solute Segregation Impedes Void Growth in Irradiated Ni-Fe Alloys, *Curr. Opin. Solid State Mater. Sci.* 23 (2019) 92–100.
- [95] R.W. Harrison, G. Greaves, H. Le, S.E. Donnelly, H. Bei, Y. Zhang, Chemical effects on He bubble superlattice formation in high entropy alloys, *Curr. Opin. Solid State Mater. Sci.* 23 (2019), 100762.
- [96] K.-Y. Tsai, M.-H. Tsai, J.-W. Yeh, Sluggish Diffusion in Co–Cr–Fe–Mn–Ni High-Entropy Alloys, *Acta Mater.* 61 (2013) 4887–4897.
- [97] E. Zarkadoula, M. Toulemonde, W.J. Weber, Additive effects of electronic and nuclear energy losses in irradiation-induced amorphization of zircon, *Appl. Phys. Lett.* 107 (2015), 261902.
- [98] Y. Zhang, R. Sachan, O.H. Pakarinen, M.F. Chisholm, P. Liu, H. Xue, W.J. Weber, Ionization-induced annealing of pre-existing defects in silicon carbide, *Nat. Commun.* 6 (2015) 8049.
- [99] L. Nuckols, M.L. Crespillo, C. Xu, E. Zarkadoula, Y. Zhang, W.J. Weber, Coupled effects of electronic and nuclear energy deposition on damage accumulation in ion-irradiated SiC, *Acta Mater.* 199 (2020) 96–106.
- [100] G. Velisa, E. Zarkadoula, D. Iancu, M.D. Mihai, C. Grygiel, I. Monnet, B. Kombaiah, Y. Zhang, W.J. Weber, Near-surface modification of defective KTaO<sub>3</sub> by ionizing ion irradiation, *J. Physics D: Applied Physics* 54 (2021), 375302.
- [101] Y. Zhang, T. Varga, M. Ishimaru, P.D. Edmondson, H. Xue, P. Liu, S. Moll, F. Namavar, C. Hardiman, S. Shannon, W.J. Weber, Competing effects of electronic and nuclear energy loss on microstructural evolution in ionic-covalent materials, *Nucl. Instr. and Meth. B* 327 (2014) 33–43.
- [102] F. E. Wang, Bonding Theory for Metals & Alloys. Copyright © 2005 Elsevier B.V. All rights reserved. (2005). ISBN-10: 0444519785, ISBN-13: 978-0444519788.
- [103] L. Qi, Effects of Electronic Structures on Mechanical Properties of Transition Metals and Alloys, *Comp. Mater. Sci.* 163 (2019) 11–16.
- [104] Y. Zhang, M. Ishimaru, T. Varga, T. Oda, C. Hardiman, H. Xue, Y. Katoh, S. Shannon, W.J. Weber, Nanoscale Engineering of Radiation Tolerant Silicon Carbide, *Phys. Chem. Chem. Phys.* 14 (2012) 13429–13436.